

Thesis for the degree of Licentiate of Engineering

# On the Character of Active Sites in Copper Exchanged Zeolites during $\text{NH}_3$ -SCR

Lin Chen



# CHALMERS

Department of Physics  
Chalmers University of Technology  
Gothenburg, Sweden 2017

On the Character of Active Sites in Copper Exchanged Zeolites during NH<sub>3</sub>-SCR  
Lin Chen

© Lin Chen, 2017

Department of Physics  
Chalmers University of Technology  
SE-412 96 Gothenburg  
Sweden  
Telephone: +46 (0)31-772 1000

Cover:

Fragment of a Cu-CHA framework with the Cu(NH<sub>3</sub>)<sub>2</sub><sup>+</sup> complex pairs inside the large cage of CHA.

Printed at Chalmers Reproservice  
Gothenburg, Sweden 2017

Lin Chen

Department of Physics

Chalmers University of Technology

## Abstract

Nitrogen oxides (NO<sub>x</sub>) are formed during combustion in diesel engines and one current approach to reduce NO<sub>x</sub> to N<sub>2</sub> is selective catalytic reduction with NH<sub>3</sub> as reducing agent (NH<sub>3</sub>-SCR). To acquire both high activity and selectivity, the active site is often atomically dispersed metal atom, so-called single-site catalysts. In the case of NH<sub>3</sub>-SCR, one example is Cu-exchanged chabazite (Cu-CHA). This is a kind of ion-exchanged zeolites that over the past decade has emerged as a promising candidate for NH<sub>3</sub>-SCR thanks to its good performance over a wide temperature window (473-773 K) and a high hydrothermal stability. In this thesis, the mechanisms for solid-state ion exchange of copper into CHA and activation of oxygen during NH<sub>3</sub>-SCR in Cu-CHA have been studied through density functional theory (DFT) in combination with ab-initio thermodynamics and molecular dynamics. Firstly, the energetic conditions for functionalization of CHA with copper ions from Cu<sub>2</sub>O(111) via the formation of Cu(NH<sub>3</sub>)<sub>2</sub><sup>+</sup> are explored. It is found that the diamine complexes form easily on Cu<sub>2</sub>O(111) and diffuse with low barriers over the surface and inside the CHA framework. The charge neutrality of the systems is maintained via counterdiffusion of H<sup>+</sup> in the form of NH<sub>4</sub><sup>+</sup> from the zeolite to the Cu<sub>2</sub>O surface where water can be formed. The efficient solvation of Cu<sup>+</sup> and H<sup>+</sup> by ammonia renders the ion-exchange process exothermic. The dynamic character of Cu ion sites in CHA in the presence of ammonia is also highlighted.

Secondly, the activation of oxygen, one crucial step during NH<sub>3</sub>-SCR reactions, is investigated. The character of ligand-solvated Cu ions under SCR conditions is explored and Cu(NH<sub>3</sub>)<sub>2</sub><sup>+</sup> is found to be the preferable species under low-temperature operation conditions (below 523 K). Direct dissociation of O<sub>2</sub> is found to be facile over a pair of Cu(NH<sub>3</sub>)<sub>2</sub><sup>+</sup>, whereas dissociation on a single Cu(NH<sub>3</sub>)<sub>2</sub><sup>+</sup> species is unlikely due to a high activation energy. The effect of Al distribution on the stability of the pair formation in CHA is also investigated. The Al distribution is found to strongly affect the propensity to form the pairs in CHA. At temperatures above 623 K, copper sites are preferably framework-coordinated without any ligands. In this case, the NH<sub>3</sub>-SCR catalytic cycle is completed over framework-coordinated Cu sites. The character of active sites during NH<sub>3</sub>-SCR is consequently condition-dependent, where the low temperature reaction occurs on Cu-solvated species. The NH<sub>3</sub>-SCR process in Cu-CHA is consequently just at the border between homogeneous and heterogeneous catalysis.

**Keywords:** NH<sub>3</sub>-SCR, SSIE, Cu-SSZ-13, Chabazite, O<sub>2</sub>-activation, O<sub>2</sub>-dissociation, Al-distribution



# List of Publications

This thesis is based on the following appended papers:

## I.

### **Mechanism for Solid-State Ion Exchange of Cu into Zeolites**

L. Chen, J. Jansson, M. Skoglundh and H. Grönbeck

*The Journal of Physical Chemistry C*, **120** (2016), 29182–29189

## II.

### **Activation of Oxygen on $(\text{NH}_3\text{-Cu-NH}_3)^+$ in $\text{NH}_3\text{-SCR}$ over Cu-CHA**

L. Chen, H. Falsig, T.V.W. Janssens and H. Grönbeck

*Submitted to Journal of Catalysis*

## III.

### **The Effect of Al-distribution on the Activation of Oxygen in $\text{NH}_3\text{-SCR}$ over Cu-CHA**

L. Chen, H. Falsig, T.V.W. Janssens, J. Jansson, M. Skoglundh and H. Grönbeck

*In manuscript*



# **My contributions to the publications**

## **Paper I**

I performed all the calculations and wrote the first draft of the paper, which was finalized together with my coauthors.

## **Paper II**

I performed all the calculations and wrote the first draft of the paper, which was finalized together with my coauthors.

## **Paper III**

I performed all the calculations and wrote the first draft of the paper, which was finalized together with my coauthors.



# Contents

<b>1</b>	<b>Introduction</b>	<b>1</b>
1.1	Single-site catalysis . . . . .	1
1.2	Ion-exchanged zeolites . . . . .	2
1.3	NH <sub>3</sub> -SCR application . . . . .	4
1.4	Objectives of this thesis . . . . .	4
<b>2</b>	<b>Electronic structure calculations</b>	<b>7</b>
2.1	The Schrödinger equation . . . . .	7
2.2	The Hartree-Fock approach . . . . .	8
2.3	Density functional theory . . . . .	9
2.3.1	A new variable—the electron density . . . . .	9
2.3.2	The Hohenberg-Kohn theorems . . . . .	10
2.3.3	The Kohn-Sham equations . . . . .	11
2.3.4	Generalized-gradient approximation (GGA) . . . . .	11
2.3.5	Hybrid functionals . . . . .	13
2.3.6	Bayesian error estimation functional (BEEF) . . . . .	13
2.3.7	Solving the Kohn-Sham equations . . . . .	14
<b>3</b>	<b>Experimental observables from DFT</b>	<b>15</b>
3.1	Structural optimization . . . . .	15
3.2	Vibrational analysis . . . . .	16
3.3	Thermodynamic analysis . . . . .	17
3.4	Transition state search . . . . .	19
3.5	Free energy simulation . . . . .	20
3.5.1	Ab-initio molecular dynamics . . . . .	20
3.5.2	Thermodynamic integration of free-energy gradients . . . . .	22
<b>4</b>	<b>The character of Cu during SSIE and NH<sub>3</sub>-SCR</b>	<b>25</b>
4.1	Mechanism for solid-state ion-exchange of Cu <sup>+</sup> in zeolites . . . . .	25
4.2	Activation of oxygen in NH <sub>3</sub> -SCR over Cu-CHA . . . . .	28
4.3	The effect of Al-distribution on Cu <sup>+</sup> -pairs formation . . . . .	32
4.4	The dynamic character of Cu sites in CHA . . . . .	35
<b>5</b>	<b>Conclusion and outlook</b>	<b>37</b>
	<b>Acknowledgments</b>	<b>39</b>



# Chapter 1

## Introduction

Catalysis has played an essential role in society since its discovery in the late eighteenth century. Catalysts are crucial in a range of areas such as production of chemicals, fuel synthesis and emission control. The German chemist Wilhelm Ostwald was the first to precisely define a catalyst in the beginning of the 20th century.<sup>1</sup> A catalyst modifies the rate at which a chemical reaction occurs, without being a part of the end products. Catalysis is generally classified as either homogeneous or heterogeneous. In homogeneous catalysis, the reactants and products are in the same phase as the catalyst, being usually a liquid. In heterogeneous catalysis, the catalyst is in a different phase from the reactants and products.<sup>2</sup> Given the important role of catalysis, considerable efforts have been made to understand the fundamental mechanisms. With increasingly improved analytical techniques, catalytic phenomenon have been explored at the atomic level using both experimental and theoretical methods. One important concept in catalysis is that of the active site. The concept was firstly introduced by Hugh Taylor<sup>3</sup> and states that it is only some particular atoms in the catalyst that are responsible for the main part of the activity.<sup>4</sup> In addition to activity, catalysts are also characterized with respect to the ability to direct the reaction to particular products. This is called the selectivity of a catalyst. In order to achieve high activity and high selectivity, it is desirable to understand the structure and composition of the active site. There are several approaches to tailor the activity and selectivity for a catalyst, and single-site catalysis is one of the choices.

### 1.1 Single-site catalysis

The usual definition of a single-site heterogeneous catalyst (SSHC) is a catalyst constituted by a metal atom, an ion, or a small atomic cluster, supported on a rigid framework.<sup>5</sup> These sites are isolated inside or at the surface of the hosting structure and act as the active sites for the chemical reactions. As the active sites are spatially separated from each other, each site interacts with adsorbates in a similar way,<sup>6</sup> which makes it performing as an isolated-site homogeneous catalyst. One substantial difference between single-site homogeneous and heterogeneous catalysts is the absence of a ligand sphere in SSHC.<sup>7</sup> The active sites of a SSHC are usually functionalized with special geometric shape, which limits the orientation of the adsorbates and gives a high stereoselectivity. For example, CO<sub>2</sub> electroreduction on a single transition metal atom anchored on defective graphene with single or double vacancies can have significant activity and selectivity thanks to the lack of an atomic ensemble for alternative adsorbate binding, which is the case with conventional transition metal surface.<sup>8</sup> Another example is the anchoring of Pd atoms in the cavities of mesoporous polymeric graphitic carbon nitride. This catalyst has a high activity and selectivity in comparison with catalysts based on nanoparticles.<sup>9</sup> The high

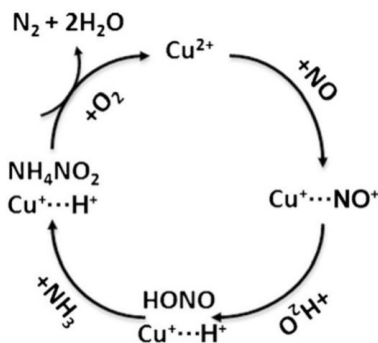


Figure 1.1: A proposed schematic mechanism for the selective catalytic reduction of NO with  $\text{NH}_3$  over Cu-SSZ-13.<sup>14</sup> Reprinted by permission from Ref [14].

activity and selectivity comes from the facile hydrogen activation and alkyne adsorption on the atomically dispersed Pd sites, which in this case inhibit the adsorption of potential poisons *e.g.* CO molecules.<sup>9</sup>

The first example of SSHCs was the pioneering work by Ballard<sup>10</sup> when single-site (transition metals Cr and Ti) silica supported systems were found to have promising results for polymerization of olefins. Later in 1980s and 1990s, porous zeolitic aluminosilicates and porous aluminophosphates, with isolated heteroatoms (other than Si, Al and P) showed good performance in n-butane<sup>11</sup> and n-octane cracking<sup>12</sup>. Over the past decades, a range of single-site catalysts have been discovered and generally those catalysts have single-site centers uniformly dispersed over inorganic, organic or composite host matrixes.<sup>13</sup> The reaction mechanism for these SSHCs is normally based on a redox cycle, where the active site changes oxidation state.

In this thesis, we show an example of a proposed mechanism for the selective catalytic reduction of NO with  $\text{NH}_3$  ( $\text{NH}_3$ -SCR) in the presence of excess  $\text{O}_2$  over Cu-SSZ-13. SSZ-13 is related to mineral chabazite, see Figure 1.1.<sup>14</sup> In this mechanism, the well-dispersed copper ions act as the active site and a redox cycle is present where the metal site changes the oxidation state between  $\text{Cu}^+$  and  $\text{Cu}^{2+}$ .

## 1.2 Ion-exchanged zeolites

Zeolites are crystalline solid structures made of silicon, aluminum and oxygen that form a framework with cavities and channels where cations, water and/or small molecules may reside.<sup>15</sup> They are often also referred to as molecular sieves. Zeolites are made of  $\text{SiO}_4$  and  $\text{AlO}_4$  tetrahedrons linked to each other by sharing the oxygen atoms to form regular cavities and channels. The difference in oxidation states between silicon and aluminum ( $\text{Si}^{4+}$  versus  $\text{Al}^{3+}$ ) requires one counter ion per  $\text{Al}^{3+}$ , for example a proton  $\text{H}^+$ , to maintain the charge neutrality. The compensation of the charge by a proton generates the Brønsted acidity. Different metal cations are introduced into zeolites by ion-exchange methods, which is generally the way to functionalize zeolites. The exchanged metal

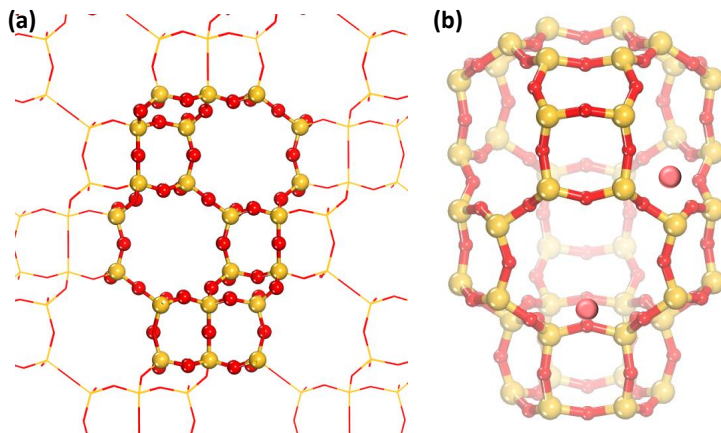


Figure 1.2: (a) Fragment of a CHA framework with atoms forming the large and one small cavity, respectively. (b) The large and small cavity with the most probable sites for Cu ions. Color code: Si-yellow, O-red, Cu-orange.

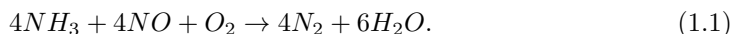
cations create Lewis acidity of the catalyst. Transition metal ion-exchanged zeolites have been extensively studied for various organic or inorganic transformations such as direct conversion of methane to methanol (Fe,Co,Ni,Cu exchanged in ZSM-5)<sup>16</sup>, epoxidation of alkenes (Mn-beta, Mn-Y, Mn-ZSM-5)<sup>17</sup>, oxidative dehydrogenation of propane (Na-Y)<sup>18</sup> and reduction of NO by NH<sub>3</sub> (Fe-ZSM-5, Cu-LTA, Cu-SSZ-13)<sup>14;19;20</sup>.

Concerning zeolites in emission control applications, zeolites like Beta (\*BEA framework), ZSM-5 (MFI framework) and SSZ-13 (CHA framework)<sup>1</sup> have been extensively studied. These zeolites have different pore window sizes and maximum molecule dimensions within the cages. CHA has a small pore window (eight-membered ring windows) size of  $3.8 \times 4.2$  Å.<sup>15</sup> SSZ-13 is a synthetic small-pore size zeolite with Chabazite (CHA) structure that over the past years has emerged as an efficient catalyst for direct conversion of methane to methanol<sup>21</sup> and selective reduction of NO<sub>x</sub> with ammonia when ion-exchanged with copper ions<sup>14</sup>. This zeolite is composed of large and small cages with 36 and 12 tetrahedra sites, respectively. The large cages are constituted by four-, six-, and eight-membered rings, whereas the small cages are made up of four- and six-membered rings, see Figure 1.2.

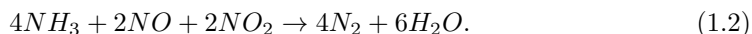
<sup>1</sup>In this thesis, CHA and SSZ-13 are used interchangeable.

### 1.3 NH<sub>3</sub>-SCR application

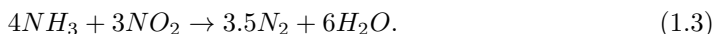
Nitrogen oxides (NO<sub>x</sub>) are formed during combustion in diesel engines and a main challenge in automotive emission control is the conversion of NO<sub>x</sub> to N<sub>2</sub> in oxygen excess. Many efforts have been made to minimize NO<sub>x</sub> emission either by combustion control or by abatement control using an aftertreatment system. The development of NO<sub>x</sub>-aftertreatment systems with high activity and durability is enforced by increasingly stricter legislations.<sup>14</sup> Although NO<sub>x</sub> reduction from gasoline engines is efficiently removed by the three-way catalyst (TWC)<sup>22;23</sup>, this technology is not suitable for a diesel engine as the TWC-technology is based on stoichiometric air/fuel conditions. There are mainly two approaches to convert NO<sub>x</sub> into harmless gas in oxygen excess, namely NO<sub>x</sub> storage and reduction (NSR) and selective catalytic reduction (SCR) by different reducing agents (hydrocarbons or NH<sub>3</sub>). The NSR catalyst is used in an engine that operates alternatively under lean and rich conditions. During lean operation, the NO<sub>x</sub> in the exhaust gas are stored on the catalyst, and during rich operation the stored NO<sub>x</sub> is reduced to nitrogen.<sup>24</sup> Nowadays, the most promising approach to remove NO<sub>x</sub> from lean burn exhausts is selective catalytic reduction with NH<sub>3</sub> as reducing agent (NH<sub>3</sub>-SCR).<sup>25;26</sup> It is known that the NO is main exhaust gas from diesel engines with only a minor fraction of NO<sub>2</sub><sup>27</sup>. Therefore, the standard NH<sub>3</sub>-SCR reaction<sup>26</sup> is:



When a mixture of NO and NO<sub>2</sub> is 1:1, it will undergo the so-called fast NH<sub>3</sub>-SCR reaction<sup>20</sup>:



If the NO:NO<sub>2</sub> ratio is below 0.5, an SCR reaction with pure NO<sub>2</sub> may take place<sup>27</sup>:



Vanadia V<sub>2</sub>O<sub>5</sub> supported on titania was the first NH<sub>3</sub>-SCR catalyst for exhaust-control application.<sup>28</sup> This SCR catalyst is active around 550-700 K. Although vanadia-based catalysts have been commercialized, it has several disadvantages such as undesired oxidation of SO<sub>2</sub> to SO<sub>3</sub> by V<sub>2</sub>O<sub>5</sub> and the low selectivity at high temperatures.<sup>29</sup> This has enforced the development of alternative SCR catalysts. Cu/Fe-exchanged zeolites are examples of such catalysts which have received extensive attention in the past decades. There are several types of zeolites used for NH<sub>3</sub>-SCR applications and the most common ones are \*BEA<sup>30</sup>, MFI<sup>20</sup> and CHA<sup>26</sup>. In particular, Cu exchanged CHA, such as Cu-SSZ-13<sup>26</sup>, have shown high NO<sub>x</sub> conversion of 90-100% over a wide temperature window (473-773 K) and the activity exceed 80% even after extensive high-temperature hydrothermal aging.<sup>14;26</sup>

### 1.4 Objectives of this thesis

As the activity and stability of the Cu-SSZ-13 catalysts for NH<sub>3</sub>-SCR reaction is determined by the Cu-ions in the zeolite framework, it is important to study the nature of the Cu

ions during the reaction. Generally, the  $\text{NH}_3$ -SCR activity of Cu-SSZ-13 originates from changes in oxidation state between  $\text{Cu}^+$  and  $\text{Cu}^{2+}$ .<sup>31</sup> Kwak *et. al*<sup>25</sup> proposed that the Cu ions primarily occupy the sites in the six-membered rings at low ion-exchange level but could also be found in the large eight-membered rings at high ion-exchange level, see Figure 1.2(b). Later, the interaction of  $\text{NH}_3$  with Cu ions in Cu-SSZ-13 was studied and it was found that Cu was solvated by  $\text{NH}_3$  during  $\text{NH}_3$ -SCR.<sup>32;33</sup> The coordination of Cu to  $\text{NH}_3$  makes the Cu species mobile and revises the understanding of the active sites in Cu-zeolites during  $\text{NH}_3$ -SCR reactions.

In this thesis, the character of Cu sites in Cu-SSZ-13 during  $\text{NH}_3$ -SCR condition is explored by theoretical methods. The methods used in this thesis are described in detail in Chapter 2 and Chapter 3. The mechanism for  $\text{Cu}^+$  exchanged into zeolites is investigated in Chapter 4 together with the mechanism for  $\text{O}_2$  activation and dissociation. The effects from Al-distribution on the Cu complex formation is also discussed in Chapter 4. The thesis is concluded by a summary and an outlook in Chapter 5.



# Chapter 2

## Electronic structure calculations

”

*We cannot know both the position and momentum of a quantum particle. If we know the momentum then we do not know the position, and visa versa, if we know the position then we do not know the momentum.*

— Werner Heisenberg<sup>34</sup>

To understand materials and chemical reactions, understanding electronic structure is fundamental as electrons are the “quantum glue” that hold the nuclei together forming chemical bonds.<sup>35</sup> It is the redistribution of electrons that enable bond breaking and bond making. Electrons can not be treated by classical Newtonian mechanics as classical mechanics is not suitable for explaining the behaviour of electrons.<sup>36</sup> About one century ago, the development of quantum mechanics showed that all objects have the character of both a particle and a wave.<sup>37</sup> A fundamental idea in quantum mechanics is that particles can be described by wave functions and that the state of a system is described by the evolution of this wave function.<sup>36</sup>

In this chapter, methods of electronic structure calculations, will be reviewed. There are two main ways to perform electronic structure calculations. The total energy of the system is either calculated by approximations of the many body wave function or the electron density. An accurate description of the electronic wave function is very demanding, which has lead to methods instead using the electronic density.

### 2.1 The Schrödinger equation

The time evolution of a system can be calculated by the time-dependent Schrödinger equation.<sup>38</sup> This is the basic equation in non-relativistic quantum mechanics:

$$\hat{H}\Psi = i\frac{\partial\Psi}{\partial t}. \quad (2.1)$$

Here  $\hat{H}$  is the Hamilton operator and  $\Psi$  is the wave function. The physical interpretation of the wave function is that the square modulus ( $|\Psi|^2$ ) represents the probability density for the system to be found within some region of the multi-dimensional space. Therefore, the integral of  $|\Psi|^2$  over the entire space is N. The Hamilton operator is the sum of the kinetic and potential energy operators, which for one particle is:

$$\hat{H} = -\frac{\hbar^2}{2m}\nabla^2 + U(\mathbf{r}, t) \quad (2.2)$$

For the system with time-independent potential energy operators, the Hamiltonian becomes time-independent. In this case, the variables of time and space in the time-dependent Schrödinger equation will be separated, which gives the time-independent Schrödinger equation:

$$\hat{H}\Psi = E\Psi \quad (2.3)$$

The Hamiltonian for a many-body system consisting of nuclei and electrons can be written in atomic units<sup>1</sup> as:

$$\hat{H} = -\sum_I \frac{1}{2M} \nabla_{\mathbf{R}_I}^2 - \frac{1}{2} \sum_i \nabla_{\mathbf{r}_i}^2 + \frac{1}{2} \sum_{\substack{I,J \\ I \neq J}} \frac{Z_I Z_J e^2}{|\mathbf{R}_I - \mathbf{R}_J|} + \frac{1}{2} \sum_{\substack{i,j \\ i \neq j}} \frac{e^2}{|\mathbf{r}_i - \mathbf{r}_j|} - \sum_{I,i} \frac{Z_I e^2}{|\mathbf{R}_I - \mathbf{r}_i|} \quad (2.4)$$

where the first and second term are the kinetic energies of nuclei and electrons, respectively, the latter three terms stand for the potential energy of nucleus-nucleus Coulomb interaction, electron-electron Coulomb interaction and nucleus-electron Coulomb interaction, respectively.

The wave function is generally unknown and has to be approximated. The energy of a system with an approximate wave function can be calculated from the expectation value of the Hamilton operator by using the variational principle.<sup>39;40</sup>

## 2.2 The Hartree-Fock approach

Considering that the mass of a nuclei is at least 1800 times larger than that of an electron, the electrons move much faster than the nucleus. Therefore, we can treat the electrons as moving in a stationary external potential from nuclei. This is the so-called Born-Oppenheimer (BO) approximation<sup>41</sup>, where the electronic wave function is separated from the nuclei wave function. Solving the electronic Schrödinger equation gives the corresponding potential energy surface with respect to the positions  $\mathbf{R}$  of the nuclei. However, it is still complicated to deal with the many-electron system. In fact, the Schrödinger equation can only be solved exactly for one-electron systems like hydrogen. One starting point for the solutions to many-electron systems is the Hartree-Fock method.<sup>36</sup> In this method, the interactions from the other electrons are taken into account in an average way. Each electron is described by an orbital and the total wave function of a system with a set of electrons can be written as a product of each independent orbital<sup>42</sup>:

$$\Psi(r_1, \dots, r_{N_e}) = \prod_{i=1}^{N_e} \psi_i(r_i) \quad (2.5)$$

which is known as a Hartree product.

<sup>1</sup>Atomic units (au or a.u.) form a system of natural units which is especially convenient for atomistic calculations. There are four fundamental constants forming the basis of the atomic units, *i.e.* mass of electron  $m_e$ , charge of an electron  $e$ , reduced Planck's constant  $\hbar$  and Coulomb force constant  $4\pi\epsilon_0$ . These are put to unity when atomic units are used.

As the electrons obey the Pauli exclusion principle, the total electronic wave function must be antisymmetric (change sign upon interchanging any two electron coordinates). Slater determinants are used to construct this type of wave functions<sup>35</sup> which is called the Fock approximation. For a general system with  $N$  electrons and  $N$  spin-orbitals, the Slater determinant is given by:

$$\Psi = \frac{1}{\sqrt{N!}} \begin{vmatrix} \psi_1(1) & \psi_2(1) & \cdots & \psi_N(1) \\ \psi_1(2) & \psi_2(2) & \cdots & \psi_N(2) \\ \vdots & \vdots & \ddots & \vdots \\ \psi_1(N) & \psi_2(N) & \cdots & \psi_N(N) \end{vmatrix}. \quad (2.6)$$

The one-electron wave function in a many-electron system needs to satisfy the following differential equation:

$$\begin{aligned} \left[ -\frac{1}{2}\nabla^2 - \sum_i^{N_n} \frac{Z_I}{|\mathbf{r}_i - \mathbf{R}_I|} \right] \psi_i(\mathbf{r}) + \sum_{j \neq i} \int \frac{|\psi_j(\mathbf{r}')|^2}{|\mathbf{r} - \mathbf{r}'|} \psi_i(\mathbf{r}) d\mathbf{r}' \\ - \sum_{j \neq i} \int \frac{\psi_j^*(\mathbf{r}') \psi_i(\mathbf{r}')}{|\mathbf{r} - \mathbf{r}'|} \psi_j(\mathbf{r}) d\mathbf{r}' = \varepsilon_i \psi_i(\mathbf{r}) \end{aligned} \quad (2.7)$$

where the third and fourth term to the left is the electron-electron Coulomb and the exchange interaction, respectively. By employing the variational principle<sup>40</sup>, the ground state wave function  $\Psi_0$  being a single Slater determinant, which corresponds to the ground state energy  $E_0$  of a system, can be obtained.<sup>35</sup> The Hartree-Fock equations are determined by their own solutions, and thus, the Hartree-Fock equations must be solved iteratively (Self-consistent field method).<sup>36</sup>

The Hartree-Fock method describes electron-electron repulsion in an average way but neglects the correlation between the electrons, which is required for an accurate description of the ground state energy.

## 2.3 Density functional theory

Over the past few decades, density functional theory (DFT) has proved to be an efficient method for large scale electronic structure calculations. The basic concept of DFT theory is to construct functionals connecting the total energy with the electron density. The introduction of electron density significantly reduce the  $3N$  degrees of freedom to only three spatial coordinates compared with using many-body wave functions. The accuracy and applicability has made DFT the method of choice in the theory of materials and heterogenous catalysis.

### 2.3.1 A new variable—the electron density

The DFT method originates from the Thomas-Fermi (TF) model proposed by Thomas<sup>43</sup> and Fermi<sup>44</sup> in 1927. In the TF theory, the kinetic energy of electrons in the system

is modeled as a functional of the electron density, where the electrons are idealized as non-interacting particles in a homogeneous electron gas. Exchange as well as correlation is neglected in this model. In 1930, Dirac added a term for the exchange in the TF model<sup>45</sup>, which gives the energy functional for electrons in an external potential  $V_{ext}(\mathbf{r})$ :

$$E_{TFD}[n(\mathbf{r})] = C_1 \int n(\mathbf{r})^{5/3} d\mathbf{r} + \int V_{ext}(\mathbf{r})n(\mathbf{r})d\mathbf{r} + C_2 \int n(\mathbf{r})^{4/3} d\mathbf{r} + \frac{1}{2} \int \int \frac{n(\mathbf{r})n(\mathbf{r}')}{|\mathbf{r} - \mathbf{r}'|} d\mathbf{r}d\mathbf{r}'. \quad (2.8)$$

The first term is the local approximation to the kinetic energy of the non-interacting electrons in a homogeneous electron gas, the second term is the interaction with the external potential  $V_{ext}$ , the third term is a local exchange term and the last term is the classical electrostatic Hartree energy. The ground state density and energy can be obtained by minimizing the Thomas-Fermi-Dirac equation given in 2.8.

Although the approximations behind Thomas-Fermi approach are crude and fail to describe the atomic shell structures and binding of molecules<sup>46</sup>, it was the first step towards electronic structure calculations with the density.

### 2.3.2 The Hohenberg-Kohn theorems

The theoretical foundation for using the electron density as the basic variable was provided in 1964 by Hohenberg and Kohn<sup>47</sup> with two remarkable theorems, which established the density functional theory. The two Hohenberg-Kohn (HK) theorems are:

**HK theorem 1** states that the external potential  $V_{ext}(\mathbf{r})$  (except a constant) is determined uniquely by the ground state particle density  $n_0(\mathbf{r})$  for any system of interacting particles. This means the hamiltonian is completely determined by the ground state density, which implies that also the many-body wave functions for the ground state is determined by the density. Thus, all ground state properties of the system are determined by the ground state density  $n_0(\mathbf{r})$ .

**HK theorem 2** demonstrates that a universal functional  $F[n(\mathbf{r})]$  for the energy  $E[n(\mathbf{r})]$  of the density  $n(\mathbf{r})$  exists, independent of the external potential  $V_{ext}(\mathbf{r})$ . For any particular  $V_{ext}(\mathbf{r})$ , the exact ground state energy of the system is the global minimum of this functional  $F[n(\mathbf{r})]$ , and the density  $n(\mathbf{r})$  that minimizes the functional is the exact ground state density  $n_0(\mathbf{r})$ .

The Hohenberg-Kohn theorems are suitable for any system consisting of interacting particles moving in an external potential  $V_{ext}(\mathbf{r})$ . Although the Hohenberg-Kohn theorems are powerful, it is still difficult to calculate any properties of because the universal functional  $F[n(\mathbf{r})]$  is unknown. However, thanks to the Kohn-Sham ansatz<sup>48</sup> proposed in 1965, DFT became a practical tool.

### 2.3.3 The Kohn-Sham equations

The idea of the Kohn-Sham approach is to replace the original many-body system by an auxiliary independent-particle system and make sure that the auxiliary system has the same ground state density as the real system. In the auxiliary independent-particle system, the electrons are assumed to move in an effective Kohn-Sham potential  $V_{KS}(\mathbf{r})$ . The electron density of the auxiliary system is given by:

$$n(\mathbf{r}) = \sum_{i=1}^N |\psi_i(\mathbf{r})|^2. \quad (2.9)$$

For a system with  $N$  independent electrons, the ground state is obtained by solving the  $N$  one-electron Kohn-Sham equations:

$$\left(-\frac{1}{2}\nabla^2 + V_{KS}(\mathbf{r})\right)\psi_i(\mathbf{r}) = \varepsilon_i\psi_i(\mathbf{r}), \quad (2.10)$$

The universal functional  $F[n(\mathbf{r})]$  is in the Kohn-Sham approach written as

$$F[n(\mathbf{r})] = T_S[n(\mathbf{r})] + E_H[n(\mathbf{r})] + E_{XC}[n(\mathbf{r})], \quad (2.11)$$

where  $T_S[n(\mathbf{r})]$  is the non-interacting independent-particle kinetic energy,  $E_H[n(\mathbf{r})]$  is the classic Coulomb (Hartree) interaction energy of the electron density with itself and  $E_{XC}[n(\mathbf{r})]$  is the exchange-correlation energy.

The ground state energy of a many-electron system can be obtained by minimizing the energy function  $E[n(\mathbf{r})]$ , which gives:

$$\begin{aligned} V_{KS}(\mathbf{r}) &= V_{ext}(\mathbf{r}) + V_H(\mathbf{r}) + V_{XC}(\mathbf{r}) \\ &= V_{ext}(\mathbf{r}) + \frac{\delta E_H[n(\mathbf{r})]}{\delta n(\mathbf{r})} + \frac{\delta E_{XC}[n(\mathbf{r})]}{\delta n(\mathbf{r})}. \end{aligned} \quad (2.12)$$

Here  $V_{ext}(\mathbf{r})$  is the external potential related to the nuclei and other external fields.

The Kohn-Sham energy of the full interacting many-body system is given by:

$$E_{KS} = T_S[n(\mathbf{r})] + \int n(\mathbf{r})V_{ext}(\mathbf{r})d\mathbf{r} + E_H[n(\mathbf{r})] + E_{XC}[n(\mathbf{r})]. \quad (2.13)$$

The most successful part of Kohn-Sham approach is to introduce an exchange and correlation term, which contains the non-classical electrostatic interaction energy and the difference between the kinetic energies of the interacting and non-interacting systems. In this way, approximations are made to only a minor part of the kinetic energy.

### 2.3.4 Generalized-gradient approximation (GGA)

As discussed above, the exact ground state density and energy for an interacting system can be given by solving Kohn-Sham equations if the exact  $E_{XC}[n(\mathbf{r})]$  is known.  $E_{XC}[n(\mathbf{r})]$  is defined as:

$$E_{XC}[n(\mathbf{r})] = (T[n(\mathbf{r})] - T_S[n(\mathbf{r})]) + (E_{int}[n(\mathbf{r})] - E_H[n(\mathbf{r})]) \quad (2.14)$$

where the first parenthesis may be considered as the kinetic correlation energy and the last contains both non-classical correlation and exchange energy.<sup>35</sup>

A simple approach for  $E_{XC}[n(\mathbf{r})]$  is the local density approximation (LDA)<sup>47</sup>, where the electron density is assumed to be very slowly changing and therefore the  $E_{XC}[n(\mathbf{r})]$  is evaluated as a homogeneous electron gas. In LDA,  $E_{XC}^{LDA}[n(\mathbf{r})]$  is written as:

$$E_{XC}^{LDA}[n(\mathbf{r})] = \int \varepsilon_{XC}^{hom}[n(\mathbf{r})]n(\mathbf{r})d\mathbf{r}, \quad (2.15)$$

where  $\varepsilon_{XC}^{hom}[n(\mathbf{r})]$  is the exchange-correlation energy per electron in a homogeneous electron gas of density  $n(\mathbf{r})$ . This energy term can be separated into exchange and correlation parts. Despite its simplicity, LDA works well for solid systems, such as metals, where the approximation of a slowly varying electron density is reasonable. The success is related to the fact that the sum rule for the exchange-correlation hole, which must be obeyed by the real functional, is reproduced by the LDA.<sup>49</sup>

It was realized that only the local uniform density at each point is not a suitable approximation for the rapidly varying electron densities of many materials, and that the gradient of the density ( $\nabla n(\mathbf{r})$ ) needs to be considered. The first attempt along this direction was the gradient expansion approximation (GEA) suggested by Kohn and Sham<sup>48</sup>, and carried out by Herman et al.<sup>50</sup>. The GEA adds a series expansion of increasingly higher order density gradient terms to the LDA. However, the inclusion of low-order gradient corrections almost never improves on the LDA<sup>51</sup>, and higher-order corrections are difficult to calculate.

Eventually, a significant improvement in the accuracy of the evaluation of  $E_{XC}[n(\mathbf{r})]$  can be obtained by using more general functions of  $n(\mathbf{r})$  and  $\nabla n(\mathbf{r})$ , *i.e.* the generalized gradient approximations (GGAs). GGAs are often called “semi-local” functionals due to their dependence on  $\nabla n(\mathbf{r})$ . Perdew and coworkers have proposed the three most popular and widely used GGAs functionals, namely PW86<sup>52</sup> (Perdew-Wang 1986), PW91<sup>53</sup> (Perdew-Wang 1991) and PBE<sup>54</sup> (Perdew-Burke-Ernzerhof). These three functionals can be regarded as refinements of the same underlying idea. With the modified exchange-correlation functional, the exchange-correlation energy will be:

$$E_{XC}^{GGA}[n(\mathbf{r})] = \int \varepsilon_{XC}^{hom}[n(\mathbf{r})]F_{XC}[n(\mathbf{r}), \nabla n(\mathbf{r})]d\mathbf{r}, \quad (2.16)$$

where  $F_{XC}[n(\mathbf{r}), \nabla n(\mathbf{r})]$  is the enhancement factor. In the PBE functional, the enhancement factor is given by:

$$F_X^{PBE}(x) = 1 + a - \frac{a}{1 + bx^2}. \quad (2.17)$$

where  $x$  is the dimensionless gradient variable.<sup>55</sup>

GGA works generally better than LDA especially on the prediction of bond length and binding energy of molecules. However, GGA performs poorly for dealing with strongly correlated system such as transition metal oxides and rare-earth materials. For example, GGA fails to describe the band gap of  $\text{Cu}_2\text{O}$ <sup>56</sup>. These pitfalls push towards functionals beyond LDA and GGAs, such as hybrid functionals.

### 2.3.5 Hybrid functionals

The hybrid functional was first introduced by Axel Becke in 1993.<sup>57</sup> By adding Hartree-Fock exchange energy, properties such as bond lengths, binding energies and electronic band gaps can be described with higher accuracy. The exchange term in Hartree-Fock approach is:

$$E_X^{HF} = -\frac{1}{2} \sum_{i,j} \int \int \psi_i^*(\mathbf{r}) \psi_j^*(\mathbf{r}') \frac{1}{|\mathbf{r} - \mathbf{r}'|} \psi_j(\mathbf{r}) \psi_i(\mathbf{r}') d\mathbf{r} d\mathbf{r}'. \quad (2.18)$$

The linear combination of  $E_X^{HF}$  and a LDA or GGA functional defines a hybrid functional. There are several hybrid functions being widely-used, such as B3LYP<sup>55;58</sup>, PBE0<sup>59</sup> and HSE<sup>60</sup>. HSE is used in this thesis. HSE was developed based on a screened coulomb potential for the exchange interaction<sup>60</sup>:

$$E_{XC}^{wPBEh} = aE_X^{HF,SR}(w) + (1-a)E_X^{PBE,SR}(w) + E_X^{PBE,LR}(w) + E_c^{PBE}, \quad (2.19)$$

where  $a$  is a mixing parameter and  $w$  is an adjustable coefficient on the extent of short-range interactions.  $E_X^{HF,SR}(w)$  is the short range Hartree-Fock exact exchange functional.  $E_X^{PBE,SR}(w)$  and  $E_X^{PBE,LR}(w)$  are the short and long range components of the PBE exchange functional and, finally  $E_c^{PBE}$  is the PBE correlation functional. The HSE exchange-correlation functional becomes the PBE0 hybrid functional when  $w$  is 0 and is asymptotically equivalent to PBE when  $w \rightarrow \infty$ . HSE includes nonlocal Fock exchange energy only for the short-range part of the electron-electron interaction, which significantly reduces the cost compared with PBE0. For HSE06,  $a = 0.25$  and  $w = 0.2$ , the parameters have been determined by fitting to the experimental data sets.

### 2.3.6 Bayesian error estimation functional (BEEF)

The van der Waals attraction originates from the interaction between fluctuating dipoles. In this thesis, BEEF-vdW method<sup>61</sup> is used to capture van der Waals attraction. It is a GGA functional augmented with a vdW-DF2<sup>62</sup> type nonlocal correlation energy. BEEF-vdW is a semiempirical density functional, which employs Bayesian statistics and a large number of experimental datasets of molecular, surface chemical and solid state materials properties to construct the exchange-correlation functionals. Generally, the exchange-correlation energy in BEEF-vdW is given by:

$$E_{XC}^{BEEF} = \sum_{m=0}^{M_x-1} a_m E_m^{GGA-x} + \alpha_c E^{LDA-c} + (1-\alpha_c) E^{PBE-c} + E^{nl-c}, \quad (2.20)$$

where  $M_x = 30$  and the GGA exchange as well as local, semilocal and nonlocal correlation are expanded in Legendre polynomials.

BEEF-vdW has been proven to perform well in quantum chemistry and condensed matter physics applications.<sup>61</sup> A feature of BEEF-vdW is an ensemble of functionals around the optimum functional, which is used to obtain an estimate of the computational error due to the functional.

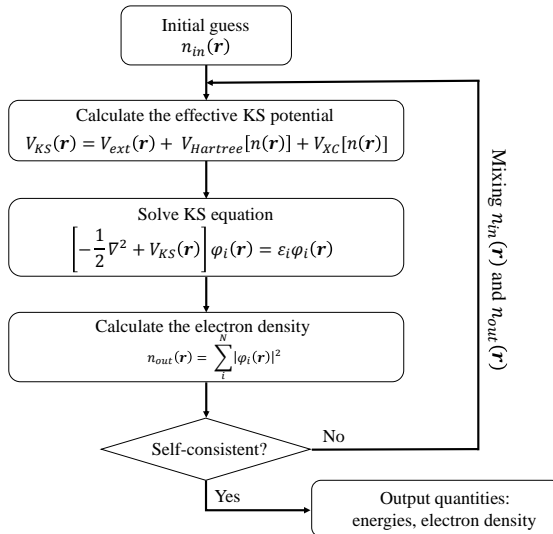


Figure 2.1: Schematic flowchart of the self-consistent loop to solve the Kohn-Sham equations. Adapted from Ref [36].

### 2.3.7 Solving the Kohn-Sham equations

The Kohn-Sham equations provide the fundamental equations to find the ground state density and ground state energy of a many-body electron problem. To solve the Kohn-Sham equations numerically, we still need a practical scheme. In this thesis, the method of plane-wave method has been employed.

In this method, the Kohn-Sham orbitals are expanded in a set of plane waves  $e^{i\mathbf{G}\cdot\mathbf{r}}$ . One advantage to use a plane wave basis set is that it, in principle, could be a complete basis set.<sup>36</sup>

The plane wave calculation needs that the wave function to be smooth and it is often smooth at chemical bonding area. However, the wave functions have wiggles near the nuclei and it is difficult to describe those fast variations using a plane wave basis.<sup>36</sup> Therefore, pseudopotentials have been developed to describe the potential of nuclei, which include the core electrons.<sup>36</sup>

In this thesis, the projector augmented wave method (PAW)<sup>63;64</sup> is used to describe the core electrons. One advantage with the PAW method is that the method keeps the entire set of all-electron core wavefunctions and the smooth parts of the valence wavefunctions.

Having the different components to solve the Kohn-Sham equations, the self-consistent Kohn-Sham equations are calculated through a self-consistent loop shown in Figure 2.1. The self-consistent loop will be terminated when the difference in total energy or electron density on each atom from the previous iterations is less than a chosen accuracy. If the difference does not satisfy the accuracy, the new electron density will be mixed with the previous electron density to continue the next iterations until it reaches the criteria.

# Chapter 3

## Experimental observables from DFT

”

*The transitory nature of some of the intermediates implicated in catalysis are such that their structures can best be ascertained by computational procedures, rather than by direct, experimental ones.*

— John Meurig Thomas & W. John Thomas<sup>65</sup>

Although recent experiments have probed the transition state in a catalytic reaction<sup>66</sup>, it is still quite demanding to detect the transitory character by experimental tools. As an alternative, the advances in first principle calculations over the past decades have allowed for atomic scale descriptions of catalytic reactions. By use of theoretical methods, it is possible to calculate measurable properties and interpret reaction mechanisms.

Figure 3.1 sketches what kind of information that can be obtained from experiments. By use of vibrational spectroscopy, such as Infrared spectroscopy or Raman spectroscopy, surface species can be detected and probed. The state of catalysts can be determined by X-ray spectroscopy and the structure can be investigated by X-ray powder diffraction. The reaction kinetics, such as reaction orders and apparent activation energies, can be determined by activity tests. The information on surface species and catalysts can also be obtained by first principles calculations. The vibrational frequencies of a species can be calculated by molecular dynamics or finite differences. The state of catalysts can be determined by electronic structure calculation and the ground state structure for a system can be obtained by doing geometry optimization. With *ab-initio* thermodynamics, the relevant structures of a system under operating conditions can be determined. The reaction barriers, which can be related to the reaction rates by the Arrhenius equation, can be calculated by the transitional state searches. Besides the energetic reaction barriers, the free energy barriers can be calculated via partition functions by vibrational analysis or explicit constrained molecular dynamics.

### 3.1 Structural optimization

One basic problem in computational chemistry is to find the arrangement of the atoms, *i.e.* geometry optimization. The process of a geometry optimization is to find a stationary point (or several stationary points) on a potential energy surface (PES), where the net force on each atom is close to zero. At a specific PES, the desired stationary point is generally a minimum, where the first derivative is zero and all the second derivative are positive.

In the common optimization methods, the gradient  $\mathbf{g}$ , *i.e.* the first derivative of

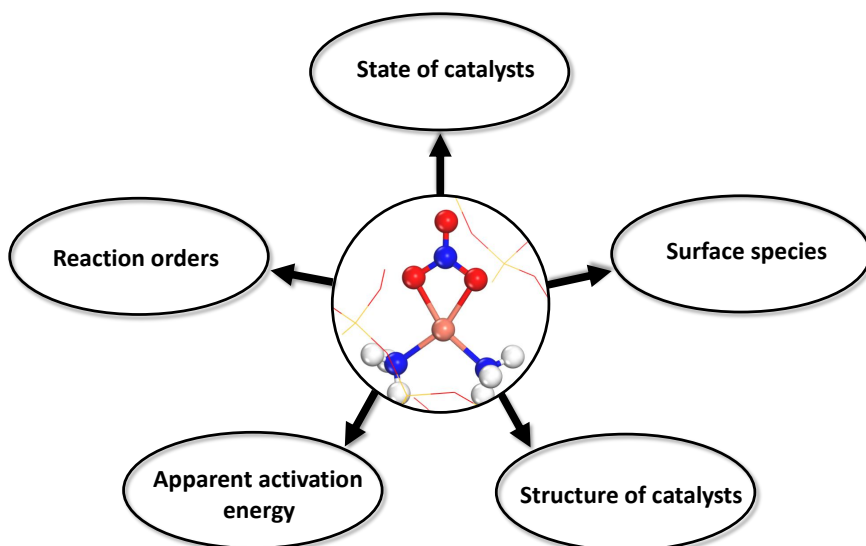


Figure 3.1: Sketch of typical information obtained from experimental studies of catalytic reactions. The species in the center of this map is a copper complex with an adsorbed nitrate.

the function with respect to all variables, can be calculated numerically. The gradient vector  $\mathbf{g}$  points the direction where the function increases most. In the Steepest Descent (SD) method, a series of steps are performed in the orthogonal gradient vector to the previous step along the search direction.<sup>35</sup> Although the SD method is easy to perform, it often converges slowly as this method may spend time minimizing the function along parallel or nearly parallel search directions. In this thesis, the conjugate-gradient (CG)<sup>67</sup> method implemented in VASP<sup>68;69</sup> is used to minimize the Kohn-Sham energy and obtain optimized structures. The CG method is an improvement with respect to the SD method as the CG method makes use of the gradient history to decide the direction of the next step.

These optimization methods basically find the nearest stationary point, but many stationary points may exist on a complicated PES. The minimum with the lowest energy value is the global minimum and the others are local minima. For some cases, it is important to sample a large set of these local minima, which is called conformational sampling. *Ab-initio* molecular dynamics is one method to do such conformational sampling.

## 3.2 Vibrational analysis

The molecular vibrations are given by the normal modes and each normal mode is in this thesis described as a harmonic oscillator in the classic treatment of molecular vibrations. This can be achieved by expanding the energy as a function of the nuclei coordinates in a Taylor series around the equilibrium position.<sup>35</sup> For a diatomic molecule, the energy is

described by the bond length  $r$ :

$$E(r) = E(r_0) + \frac{dE}{dr}(r - r_0) + \frac{1}{2} \frac{d^2E}{dr^2}(r - r_0)^2 + \frac{1}{6} \frac{d^3E}{dr^3}(r - r_0)^3 + \dots, \quad (3.1)$$

where  $r_0$  is the bond length at the equilibrium state. The first term is the ground state energy of the system. The second term is zero since the system is moving around the equilibrium position. In the harmonic approximation, the energy is:

$$E(r) = E(r_0) + \frac{1}{2} \frac{d^2E}{dr^2}(r - r_0)^2. \quad (3.2)$$

The higher order terms can be considered as anharmonic corrections to the vibration are typically only a few percent of the energy. In an  $N$ -body system, there will be  $3N$  degrees of freedom [ $\mathbf{r} = (r_1, r_2, \dots, r_{3N})$ ] and the energy will be written as:

$$E(x) = E(x_0) + \frac{1}{2} \sum_{i=1}^{3N} \sum_{j=1}^{3N} \frac{\partial^2 E}{\partial x_i \partial x_j} x_i x_j, \quad (3.3)$$

where  $x = \mathbf{r} - \mathbf{r}_0$  ( $\mathbf{r}_0$  is the system in an equilibrium state). There are  $3N \times 3N$  possible second derivatives and the matrix of these second derivatives is called Hessian matrix.

$$H(ij) = \frac{\partial^2 E}{\partial x_i \partial x_j} \quad (3.4)$$

Treating the atoms as classic particles following Newton's law and Hooke's law, the equation of the motion can be written as

$$\frac{d^2 \mathbf{x}}{dt^2} = \mathbf{A} \mathbf{x}, \quad (3.5)$$

where  $\mathbf{A}$  is mass-weighted Hessian matrix with  $A_{ij} = H_{ij}/m_i$ . The eigenvectors  $\mathbf{e}$  of this matrix and the corresponding eigenvalues  $\lambda$  are determined by  $\mathbf{A} \mathbf{e} = \lambda \mathbf{e}$ . Therefore, to obtain the normal modes from first principles calculations, the main task is to calculate the elements of Hessian matrix  $\mathbf{H}_{ij}$ . By using the finite-difference approximation, the Hessian matrix can be estimated by

$$H_{ij} = \frac{\partial^2 E}{\partial x_i \partial x_j} \approx \frac{(E(\delta x_i, \delta x_j) - E_0) - (E_0 - E(-\delta x_i, -\delta x_j))}{\delta x_i \delta x_j}. \quad (3.6)$$

With the Hessian matrix  $\mathbf{H}_{ij}$ ,  $3N$  normal mode frequencies are given by the  $3N$  eigenvalues of the mass-weighted Hessian matrix  $\mathbf{A}$ .

### 3.3 Thermodynamic analysis

The ground state properties obtained from DFT calculations are calculated at zero-temperature and zero-pressure conditions. However, most experiments are performed at a specific temperature or pressure. Thermodynamics and statistical mechanics can be used

in combination with DFT to link the microscopic regime to the macroscopic regime<sup>70;71</sup> by *ab-initio* thermodynamics. To estimate the thermodynamic variables in a statistical ensemble, partition functions are used to calculate free energies.<sup>72</sup> For a single molecule, the partition function is defined as:

$$q = \sum_i^{\infty} e^{-\beta \varepsilon_i} \quad (3.7)$$

where  $\beta$  is  $1/(k_B T)$  and  $\varepsilon_i$  is the total energy corresponding to the quantum state  $i$ . For  $N$  non-interacting particles (ideal gas), the corresponding partition function  $Q$  is  $q^N$  for independent–distinguishable particles and  $q^N/N!$  for independent–indistinguishable particles, respectively. For  $N$  interacting particles like liquid or solid state, the partition function  $Q$  must be summing over all energy states  $E_i$  for the entire system and is given by  $Q = \sum_i^{\infty} e^{-\beta E_i}$ . As the energy levels for interacting system is not discrete anymore, the partition function can be integral over the space. The thermodynamic state functions can be derived from the partition function  $Q$ , such as the internal energy  $U$ , Helmholtz free energy  $A$ , pressure  $P$ , enthalpy  $H$ , entropy  $S$  and Gibbs free energy  $G$ .<sup>35</sup>

$$\begin{aligned} U &= k_B T^2 \left( \frac{\partial \ln Q}{\partial T} \right)_V \\ A &= U - TS = -k_B T \ln Q \\ P &= - \left( \frac{\partial A}{\partial V} \right)_T = k_B T \left( \frac{\partial \ln Q}{\partial T} \right)_T \\ H &= U + PV = k_B T^2 \left( \frac{\partial \ln Q}{\partial T} \right)_V + k_B T V \left( \frac{\partial \ln Q}{\partial T} \right)_T \\ S &= \frac{U - A}{T} = k_B T \left( \frac{\partial \ln Q}{\partial T} \right)_V + k_B \ln Q \\ G &= H - TS = k_B T V \left( \frac{\partial \ln Q}{\partial T} \right)_T - k_B T \ln Q \end{aligned} \quad (3.8)$$

For an isolated molecule, the total energy can be approximated as a sum of translational, rotational, vibrational and electronic energy. This implies the partition function can be written as a product of these parts:

$$\begin{aligned} q_{tot} &= q_{trans} q_{rot} q_{vib} q_{elec} \\ H_{tot} &= H_{trans} + H_{rot} + H_{vib} + H_{elec} \\ S_{tot} &= S_{trans} + S_{rot} + S_{vib} + S_{elec}. \end{aligned} \quad (3.9)$$

The translational partition function of a molecule confined in a volume  $V$  is:

$$q_{trans} = \frac{(2\pi M k_B T)^{3/2}}{h^3} V \quad (3.10)$$

where  $M$  is the mass of the molecule.  $V$  can be related to the pressure via the ideal gas law. Within rigid-rotor approximation, the rotational partition function for a non-linear

molecule is given by:

$$q_{rot} = \frac{\sqrt{\pi}}{\sigma} \left( \frac{8\pi^2 k_B T}{h^2} \right)^{3/2} \sqrt{I_1 I_2 I_3} \quad (3.11)$$

where  $\sigma$  is the symmetry index of the molecule and  $I_x$  is the moments of inertia along three spatial axes. For a linear molecule with only two degrees of freedom to rotate, the partition function is:

$$q_{rot} = \frac{\sqrt{\pi}}{\sigma} \frac{8\pi^2 k_B T I}{h^2}. \quad (3.12)$$

The vibrational partition function for a molecule in the rigid-rotor model is given as:

$$q_{vib} = \prod_i \frac{e^{-hv_i/2k_B T}}{1 - e^{-hv_i/k_B T}} \quad (3.13)$$

where  $v_i$  is the vibration frequency of mode  $i$ .

The electronic partition function is a sum over all electronic quantum states. However, the energy difference between the ground and excited states is usually much larger than  $k_B T$ .<sup>35</sup> Thus, the electronic partition function is:

$$q_{elec} \approx g_0 e^{-E_0/k_B T}. \quad (3.14)$$

Here,  $g_0$  is the degeneracy factor.

With the above partition functions, the enthalpy and entropy terms can be calculated by using equation 3.8. Therefore, for a specific system with a single conformation, the Gibbs free energy from a DFT calculations can be derived as

$$G = E_{elec} + \Delta G_{trans} + \Delta G_{rot} + \Delta G_{vib} + \Delta G_{elec}. \quad (3.15)$$

### 3.4 Transition state search

To get the activation energy for a reaction, the transition state needs to be calculated. At a specific PES, the maximum peak is a saddle point with both negative and positive second derivatives. What we are interested in, is the first-order saddle point with only one negative  $H_{i,j}$  eigenvalue as this corresponds to the transition state (TS). The transition state connects two adjacent minima (for the reactant and the product). The energy difference between the reactant and the TS can be related to the experimentally measured apparent activation energy.

Finding the first-order saddle point, *i.e.* transition state, is generally difficult. The proposed methods can be divided into two types. One is based on the interpolation between two minima, which are corresponding to the reactant and product structures. The interpolation method assumes the TS state is located somewhere “between” the two minima. The Nudged Elastic Band (NEB)<sup>73;74</sup> method is one of this interpolation methods and has been used in this thesis. The other method is only using information about the first derivative and also second derivative at the saddle point. This approach may require a good estimate of the TS. The dimer method<sup>75</sup> is one example of this type.

## The NEB method

The NEB method is designed to find the minimum energy path (MEP) between two stable states.<sup>73;74</sup> The NEB is a chain-of-states method with a string of images (geometry configurations), which represents the reaction path. The images are connected by spring forces as 'nudging' by a spring constant  $k$  which will be distributed evenly along the path. The images along the NEB are converged to MEP. An illustration of this method is shown in Figure 3.2. The relaxation of NEB to the MEP is performed by a force projection scheme and the NEB force on image  $i$  is projected by

$$F_i^{NEB} = F_i^\perp + F_i^{SII}, \quad (3.16)$$

where  $F_i^\perp$  is the component of the force perpendicular to elastic band and  $F_i^{SII}$  is the spring force parallel to the band. The tangent  $\hat{\tau}_i$  along the path is denoted as the unit vector to the neighboring image with higher energy. During the constrained relaxation, the spring force will not interfere with the relaxation of the images perpendicular to the path and it will converge until the total force  $F_i^\perp$  is within the defined criteria. To find the saddle point, MEP can be further optimized by the climbing-image NEB (CI-NEB).<sup>76</sup> During the CI-NEB, the spring forces on the highest energy image will be removed and the force on this image will be fully decided by the potential with the component along the tangent. If the CI-NEB calculation converges, the climbing image will converge to the saddle point.

## Dimer method

Within the dimer method, two symmetrical configurations with a constant distance are considered. The centre of the dimer is defined by the vector between the two structures and this vector will estimate the lowest curvature mode. Therefore, dimer method is also called as min-mode method.<sup>75</sup> During optimization, the dimer is rotated around its center to minimize the total energies of the dimer to find the lowest curvature mode. In this way, the center of the dimer is climbing towards the lowest curvature mode direction along the PES until it is converged to the first-order saddle point.

## 3.5 Free energy simulation

To calculate the free energy of activation during a catalytic reaction, one way is to calculate the free energy difference along the reaction path. Thermodynamic integration<sup>77</sup> is one of the most popular approach to calculate the free energy difference. This method is performed during a constrained *ab-initio* molecular dynamics.

### 3.5.1 Ab-initio molecular dynamics

To model the real reaction with dynamic atoms, molecular dynamics (MD) has been employed in this work. The term *ab-initio* molecular dynamics refers to molecular dynamics simulations based on a PES from first principles by using a quantum mechanical method, such as DFT. By calculating the PES on the fly, the forces on the nuclei can

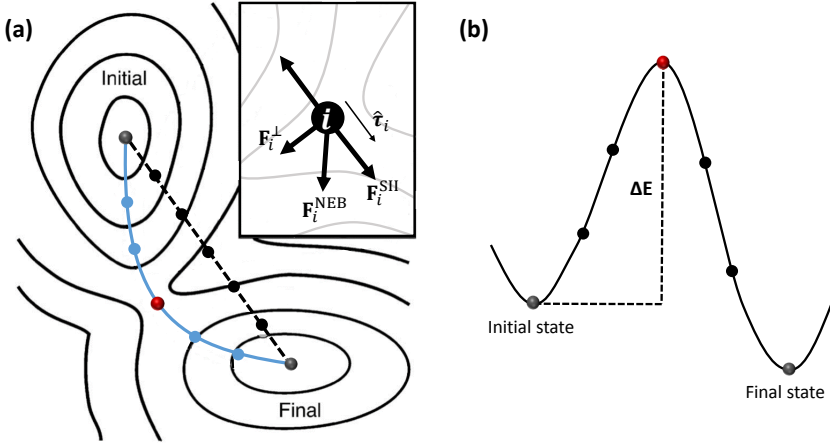


Figure 3.2: (a) Schematic picture of the nudged elastic band (NEB) method. The blue line is the minimum energy path with 5 intermediate images. (b) The potential energy profile along the minimum energy path. This figure is adapted from Ref [74].

be calculated. The motion of the nuclei is calculated by solving Newton's equations of motions:

$$M_i \frac{dv_i}{dt} = - \frac{\partial E}{\partial R_i} \quad (3.17)$$

where  $v_i$  is the velocity of the nuclei,  $M_i$  is the corresponding nuclei mass,  $R_i$  is the nuclei coordinates and  $E$  is total potential energy.

In this thesis, the molecular dynamics simulation are performed using the so-called Born-Oppenheimer Molecular Dynamics (BOMD).<sup>78</sup> The potential energy is BOMD minimized in every MD step. There is another kind of *ab-initio* molecular dynamics, called Car-Parrinello MD.<sup>79</sup> As opposed to BOMD, Car-Parrinello MD simulations treat the parameters describing the electronic wave functions as classical degrees of freedom and propagate them as such, instead of solving directly for the wave function at each time step.

During the molecular dynamics, the equation of motion are integrated numerically by use of Verlet algorithm<sup>80</sup>:

$$R_i(t + \Delta t) \approx 2R_i(t) - R_i(t - \Delta t) + \frac{dv_i(t)}{dt} \Delta t^2. \quad (3.18)$$

Without temperature control, a molecular dynamics simulation behaves as a micro-canonical ensemble (constant  $N, V, E$ ). However, under typical experimental condition,

the system is able to exchange heat with the environment. To compare the MD results with experimental observations, we would like to use the canonical ensemble with constant  $N, V, T$ . To simulate a canonical ensemble, a thermostat method is needed to control the temperature. The temperature of the system is given via the equipartition theorem:

$$\sum_i \frac{1}{2} M_i v_i^2 = \frac{3}{2} N k_B T \quad (3.19)$$

where  $T$  is the instantaneous temperature and  $N$  is the number of the nuclei. One simple way to describe the canonical ensemble was proposed by Nosé<sup>81;82</sup> by introduced an extended Lagrangian with an extra degree freedom of heat bath,  $s$ :

$$L = \frac{1}{2} \sum_i M_i s^2 v_i^2 - E + \frac{Q}{2} \left( \frac{ds}{dt} \right)^2 - g k_B T \ln(s) \quad (3.20)$$

where  $Q$  is an imaginary mass and  $g$  is the number of independent momentum degrees of freedom of the nuclei in the system. Hoover<sup>83</sup> has further improved the extended Lagrangian by introducing a friction coefficient  $\xi$ :

$$\begin{aligned} \frac{dv_i}{dt} &= -\frac{1}{M_i} \frac{\partial E}{\partial R_i} - \frac{\xi}{M_i} v_i \\ \xi &= \frac{d \ln s}{dt} \end{aligned} \quad (3.21)$$

and with this  $\xi$ , the MD simulation temperature will be controlled through:

$$\frac{d\xi}{dt} = \frac{3Nk_B}{Q} (T - T_{Target}). \quad (3.22)$$

Therefore, if the instantaneous temperature is too high,  $\xi$  will be smoothly adjusted by equation 3.22 and will directly effect the velocities of the nuclei, which will correspondingly reduce the kinetic energy of the system. This approach on controlling the temperature is known as a Nosé-Hoover thermostat.

### 3.5.2 Thermodynamic integration of free-energy gradients

The reversible work of changing a system between two states is an important quantity in statistical mechanics. The difference of free energy  $A$  between two states corresponds to the work, if this quantity is independent of the path followed the space of the thermodynamic state variables.<sup>84</sup> To calculate the free energy difference  $A$ , one of the most popular approach is thermodynamic integration.<sup>77</sup> This method has been generalized to include integration over variables  $\xi$  as a parameter of the Hamiltonian of the system:

$$\Delta A_{1 \rightarrow 2} = \int_{\xi(1)}^{\xi(2)} \left( \frac{\partial A}{\partial \xi} \right)_{\xi^*} \cdot d\xi \quad (3.23)$$

where the negative of the integrand is the mean force and  $\xi^*$  is the reaction coordinate.

Along a desired reaction path, the particular value of the reaction coordinate  $\xi$  is of low probability during a normal MD simulation. A convenient method for MD approach

is the so-called blue-moon ensemble sampling method,<sup>85</sup> where a constrained trajectory with the reaction coordinate is fixed at a specific value. During this constrained MD, the mean force can be estimated directly from the extended Lagrangian in the constrained MD trajectory with sufficient statistical precision via SHAKE algorithm.<sup>86</sup>

Therefore, the mean force, *i.e.* the free-energy gradients were determined from constrained *ab-initio* MD simulations using the equation<sup>87-90</sup>:

$$\left(\frac{\partial A}{\partial \xi_k}\right)_{\xi^*} = \frac{1}{\langle |\mathbf{Z}|^{-1/2} \rangle_{\xi^*}} \langle |\mathbf{Z}|^{-1/2} [-\lambda_{\xi_k} + k_B T G] \rangle_{\xi^*} \quad (3.24)$$

where  $k_B$  is the Boltzmann constant and  $T$  is the simulation temperature. Here,  $\mathbf{Z}$  is defined by

$$\mathbf{Z} = \sum_i \frac{1}{m_i} \left( \frac{\partial \xi}{\partial \mathbf{r}_i} \right)^2. \quad (3.25)$$

$\mathbf{Z}$  is a mass metric tensor, which can compensate the bias introduced by the constraint using this blue-moon ensemble approach.<sup>85</sup>  $G$  in 3.24 is a factor to eliminate the explicit dependence on the generalized coordinates complementary to  $\xi$ .<sup>84</sup>



# Chapter 4

## The character of Cu during SSIE and NH<sub>3</sub>-SCR

During the past five years, copper exchanged zeolites, particularly Cu-SSZ-13, have been recognized as efficient catalysts for NH<sub>3</sub>-SCR.<sup>14;91</sup> Kwak<sup>92</sup> *et al.* studied the effect of copper loading in SSZ-13 on the NO<sub>x</sub> reduction activity and the catalyst was found to be active also at low copper loadings, which suggests that the energetically preferred positions for Cu ions are active in the reaction. As the activity and stability of the catalyst are determined by the location of the Cu ions in the microporous structure of the zeolite, it is of great interests to characterize the active sites. During the recent two years, it has been found that Cu sites respond sensitively to the operating conditions and that Cu species are mobilized by NH<sub>3</sub> during SCR conditions.<sup>32;56;91;93</sup> This finding implies that modification of the reaction conditions could be an alternative way to tune the catalytic activity of functionalized zeolites and also stresses the importance of ligands-solvated Cu sites during the reaction.

In this chapter, firstly the character of the Cu<sup>+</sup> during the solid-state ion-exchange (SSIE) in zeolites is explored and the mechanism for the functionalization is elucidated. Furthermore, the detailed reaction mechanism for activation of oxygen, one important reaction in NH<sub>3</sub>-SCR, is described over Cu-CHA and the nature of the Cu-sites during this reaction is presented. Cu-pairs are found to be needed during the activation of oxygen and that the formation of Cu-pairs depends on the Al-distribution. Lastly, the dynamic character of Cu sites in CHA is shown from MD simulations.

### 4.1 Mechanism for solid-state ion-exchange of Cu<sup>+</sup> in zeolites

Ion-exchanged zeolites are traditionally synthesized via an aqueous route where metal complexes are dissolved in water and mixed with the zeolite powder. This procedure has several drawbacks as it is time-consuming and may require consecutive wash-and-dry steps to achieve the desired ion-exchange level.<sup>94;95</sup> Additionally, ion-exchange into small-pore zeolites, including chabazite may be hindered by bulky aqueous complexes<sup>96</sup> which cannot enter the zeolite cages. An alternative route for ion exchange of zeolites is the, so-called, solid-state ion exchange (SSIE) method.<sup>97;98</sup> Traditionally, the SSIE method has been used with high temperatures where a metal salt or oxide are mixed with zeolite powder and heated to 700-800 °C. Metal ions are formed during the heating and diffuse into the zeolite structure.<sup>99;100</sup> Interestingly, it was recently demonstrated that copper could be exchanged into SSZ-13 at low temperatures in the presence of ammonia.<sup>101</sup> In particular, the facile exchange could be performed at 450 °C. The SSIE method is straightforward and offer an easy way to control the metal loading in the zeolite.

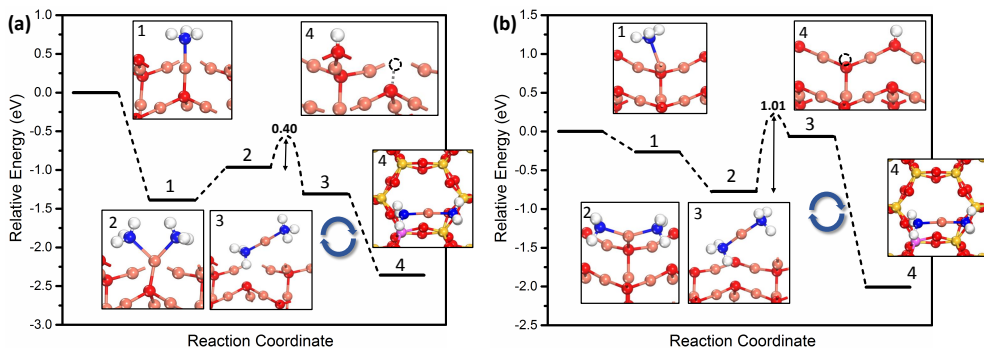


Figure 4.1: Zero-point corrected energies obtained with the HSE06 functional for the SSIE process over the two cuprous oxide surfaces with the  $p(1 \times 2)$  surface cell. (a) stoichiometric  $\text{Cu}_2\text{O}(111)$  surface and (b)  $\text{Cu}_2\text{O}(111)$  surface with two  $\text{Cu}_{\text{cus}}$  vacancies. Here, the ion-exchange energy is calculated by comparison of the relative energy of step 3 and step 4. During step 3, copper diamine is formed on  $\text{Cu}_2\text{O}(111)$ . During step 4, the copper diamine is located in SSZ-13 and the proton forms an OH-group on  $\text{Cu}_2\text{O}(111)$ .

It has on the basis of Cu K-edge XANES spectra been suggested<sup>31;32</sup> that  $\text{Cu}^+$  is diffusing in the form of a diamine complex  $\text{Cu}(\text{NH}_3)_2^+$  during SSIE process. Importantly, the structure and function of copper-exchanged SSZ-13 appear to be the same for samples prepared with either the aqueous or the SSIE method.<sup>32;101</sup> To explore the mechanisms involved in the SSIE exchange process, a model involved  $\text{Cu}_2\text{O}$  surface and CHA structure is built. Even though  $\text{CuO}$  is the stable copper oxide phase under SSIE temperature (see supporting information in Paper I), part of  $\text{Cu}^{2+}$  ions will be reduced by NO or  $\text{NH}_3$  to  $\text{Cu}^+$  ions under SCR condition.<sup>32</sup> Therefore,  $\text{Cu}_2\text{O}$  is used to provide copper-ion source instead of  $\text{CuO}$ .

Ammonia adsorption is explored on  $\text{Cu}_2\text{O}(111)$  as this is the cuprous oxide surface with the lowest surface energy.<sup>102</sup> Two kinds of  $\text{Cu}_2\text{O}(111)$  surfaces are considered, *i.e.*, the non-polar stoichiometric  $\text{Cu}_2\text{O}(111)$  (denoted as  $(111)(1 \times 2)$ ) and the unstoichiometric  $\text{Cu}_2\text{O}(111)$  with two Cu vacancies (denoted as  $(111)(1 \times 2)\text{-V}$ ). Sequential ammonia adsorption and  $\text{Cu}(\text{NH}_3)_2^+$  formation on the two types of  $\text{Cu}_2\text{O}(111)$  surfaces are shown in Figure 4.1. It can be seen that the first  $\text{NH}_3$  is adsorbed on  $(111)(1 \times 2)$  by  $-1.39$  eV and the adsorption energy of the second  $\text{NH}_3$  is endothermic by  $0.42$  eV in Figure 4.1(a). The adsorption energies have a coverage dependence and the endothermicity is reduced in the  $p(2 \times 2)$  cell. Formation of the  $\text{Cu}(\text{NH}_3)_2^+$  complex is exothermic compared with the situation of two adsorbed ammonia molecules, with a slight barrier of  $0.40$  eV. The complex is close to linear with N-Cu distances of about  $1.90$  Å. The first ammonia adsorbs weaker on the  $(111)(1 \times 2)\text{-V}$ , with an adsorption energy of  $-0.26$  eV and the adsorption of a second ammonia is clearly exothermic with the formation of a structure where the N-Cu-N axis is parallel to the surface in Figure 4.1(b). The complex is in this case formed with a barrier of  $1.01$  eV and the adsorbed complex is slightly endothermic with respect

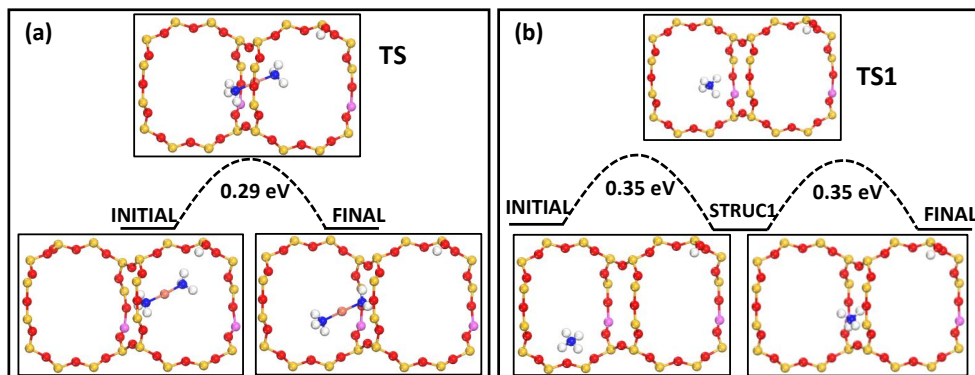


Figure 4.2: Diffusion barrier for (a) diffusion of  $\text{Cu}(\text{NH}_3)_2^+$  across an eight-membered ring and (b) ammonium diffusion across the eight-membered ring.

to the two adsorbed ammonia molecules. During the exchange step (step from 3 to 4 in Figure 4.1), the complex is moved to the zeolite and the proton moved to the cuprous oxide surface forming an OH-group. The SSIE processes are in both cases exothermic by  $-1.05$  eV for  $(111)(1 \times 2)$  and  $-1.94$  eV  $(111)(1 \times 2)\text{-V}$ . The considerably higher energy gain for the surface with vacancies is rationalized by a stronger O-H bond on this surface. The exchange of the  $\text{H}^+$  from the zeolite to the oxide surface retains a surface where the proton takes the role of  $\text{Cu}^+$ . The exchange process is further stabilized by the formation of gas phase water. It is also found that ammonium ( $\text{NH}_4^+$ ) is formed without any barrier when  $\text{NH}_3$  is allowed to structurally relax close to a proton in SSZ-13. Therefore, ammonium is assumed to be the proton carrier during the SSIE process.

Knowing that the SSIE exchange process is facile in the presence of ammonia, it becomes important to investigate possible diffusion limitations both for the complex and the ammonium in SSZ-13. The diffusion barrier for the complex  $\text{Cu}(\text{NH}_3)_2^+$  passing through the eight-membered ring is shown in Figure 4.2(a). The insets show the initial, final and transition states. The transition state calculation shows that the diffusion barrier for the complex passing through the eight-member ring is only  $0.29$  eV. The transition state is with the Cu-ion roughly in the plane of the zeolite ring. Also the diffusion of  $\text{NH}_4^+$  in SSZ-13 proceeds with low barriers. The diffusion is in this case characterized by three different steps. Ammonium is initially adsorbed in the eight-membered ring, coordinated via a hydrogen bond to an oxygen atom adjacent to  $\text{Al}^{3+}$  in a four-membered ring. In the first step, ammonium is moved from one eight-membered ring to the neighboring eight-membered ring with a barrier of  $0.35$  eV. Diffusion through the eight-membered ring has a similar barrier. So has the third step, where ammonium again diffuses between two eight-membered rings. These results show that ammonium easily can facilitate proton transport in the zeolites.

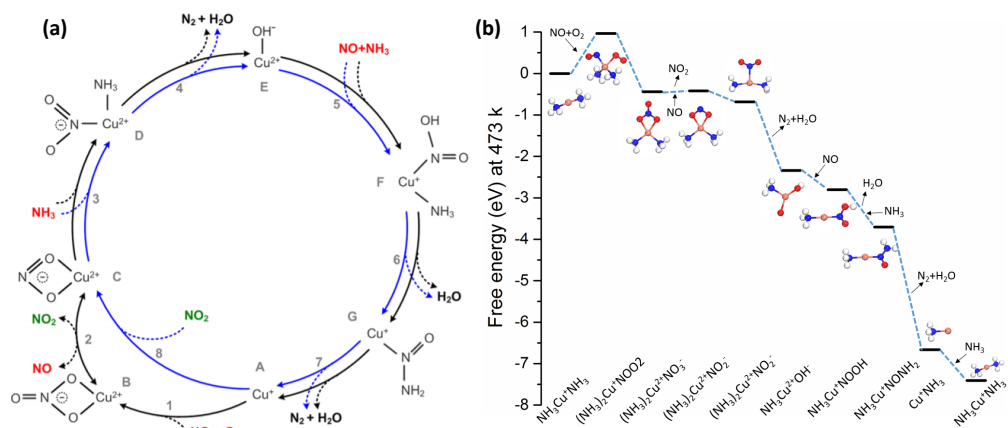


Figure 4.3: (a) A proposed NH<sub>3</sub>-SCR cycle over Cu-SSZ-13.<sup>31</sup> This figure is reprinted with permissions from Ref [31]. (b) Free energy landscape of NH<sub>3</sub>-SCR according to the proposed mechanism cycle in (a) but on Cu(NH<sub>3</sub>)<sub>2</sub><sup>+</sup> instead of framework-coordinated Cu<sup>+</sup>.

## 4.2 Activation of oxygen in NH<sub>3</sub>-SCR over Cu-CHA

In recent years, the reaction mechanism in NH<sub>3</sub>-SCR over Cu-CHA has been extensively studied via experimental and theoretical methods. Basically, a redox cycle for the NH<sub>3</sub>-SCR is fulfilled between the change of the oxidation states of Cu<sup>+</sup> and Cu<sup>2+</sup>. Regarding the reduction step Cu<sup>2+</sup> → Cu<sup>+</sup>, there seems to be a consensus that NO-assisted coordinated NH<sub>3</sub> dissociation on Cu<sup>2+</sup> reduces Cu<sup>2+</sup> to Cu<sup>+</sup>.<sup>31;91;103;104</sup> However, the elementary steps within the oxidation part (Cu<sup>+</sup> → Cu<sup>2+</sup>), particularly the activation and dissociation of O<sub>2</sub>, is still not clearly known. Recently, a full reaction scheme was proposed,<sup>31</sup> see Figure 4.3(a). However, the detailed elementary steps for activation and dissociation of O<sub>2</sub> in this cycle were not suggested.

As mentioned before, Cu sites are very sensitive to the NH<sub>3</sub> and can be solvated by NH<sub>3</sub> ligands from several experimental studies.<sup>91;93</sup> Before investigating the activation of oxygen during NH<sub>3</sub>-SCR over Cu-CHA, it is important to establish the thermodynamic stability of Cu complexes with respect to NH<sub>3</sub> partial pressure and temperature. Cu(NH<sub>3</sub>)<sub>2</sub><sup>+</sup> complexes are formed without barriers upon ammonia adsorption on a framework-coordinated Cu(I) ion.<sup>56</sup> We find that the first two NH<sub>3</sub> are strongly bonded to Cu<sup>+</sup> in the zeolite with sequential binding energies of -1.58 eV and -1.50 eV. The third and fourth NH<sub>3</sub>-ligands are, instead, weakly bonded by -0.34 eV and -0.55 eV, respectively. These results are consistent with a previous report by Paolucci *et al.*<sup>91</sup>

The phase-diagram for Cu(I) solvated by one to four ammonia ligands is shown in Figure 4.4. The corresponding structures are reported in Paper II. The analysis shows that Cu(I) is solvated preferably by two ammonia molecules forming a linear Cu(NH<sub>3</sub>)<sub>2</sub><sup>+</sup> complex

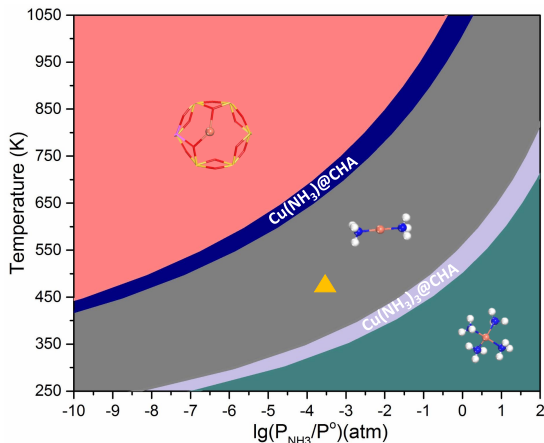


Figure 4.4: Phase diagram for  $\text{Cu}(\text{NH}_3)_x^+$  in SSZ-13 with varying  $\text{NH}_3$  pressure and temperature. Z-Cu denotes a framework-coordinated Cu(I) ion. Z-Cu-X $\text{NH}_3$  denotes Cu(I) solvated by X ammonia molecules. The yellow triangle indicates typical operating conditions, *i.e.* a temperature of 473 K and an  $\text{NH}_3$  concentration of 300 ppm. The phase-diagram is constructed with  $\text{NH}_3$  in the gas-phase as reference.

under typical  $\text{NH}_3$ -SCR conditions (473 K and 300 ppm  $\text{NH}_3$ , marked with triangle). This finding is in accordance with the work by Lomachenko *et al.*<sup>93</sup> where a combination of different experimental techniques was used to conclude that low-temperature (below 473 K)  $\text{NH}_3$ -SCR was dominated by  $\text{NH}_3$  solvated Cu-species. The results are consistent also with the phase diagram in Ref.<sup>91</sup> which was constructed with respect to  $\text{O}_2$  pressure.

The phase-diagram shows that a temperature increase leads to sequential desorption of ammonia although the region with only one ligand is narrow. Cu(I) is bonded directly to the framework at high temperatures. The phase-diagram in combination with previous experimental and theoretical work<sup>91;93</sup> confirms that the majority of copper ions in CHA under typical ammonia partial pressures and temperatures below  $\sim 500$  K are solvated by ammonia as  $\text{Cu}(\text{NH}_3)_2^+$  complexes.

Given the fact that  $\text{Cu}(\text{NH}_3)_2^+$  complexes are stable under low-temperature  $\text{NH}_3$ -SCR regimes, we adjust the reaction cycle (Figure 4.3(a)) by considering  $\text{Cu}(\text{NH}_3)_2^+$  instead of  $\text{Cu}^+$  and calculated the free energy for each step, which is shown in Figure 4.3(b). The entire reaction is exothermic except for NO and  $\text{O}_2$  adsorbed on single  $\text{Cu}(\text{NH}_3)_2^+$ , which indicates that it could be difficult to dissociate  $\text{O}_2$  on the single  $\text{Cu}(\text{NH}_3)_2^+$ . This is also addressed in other work.<sup>91;104;105</sup> We calculated the direct dissociation of  $\text{O}_2$  on single  $\text{Cu}(\text{NH}_3)_2^+$  in CHA and it is found that it is improbable to dissociate  $\text{O}_2$  on a single complex. Pairs of copper sites have previously been suggested to be important for the reaction<sup>91;104;106;107</sup> and as the  $\text{Cu}(\text{NH}_3)_2^+$  complexes are mobile, it is conceivable to form pairs of  $\text{Cu}(\text{NH}_3)_2^+$  complexes.

In contrast to the  $\text{O}_2$  dissociation on a single  $\text{Cu}(\text{NH}_3)_2^+$ , the pairs of  $\text{Cu}(\text{NH}_3)_2^+$  provide a possibility to dissociate  $\text{O}_2$ . Figure 4.5(a) shows the proposed path for direct

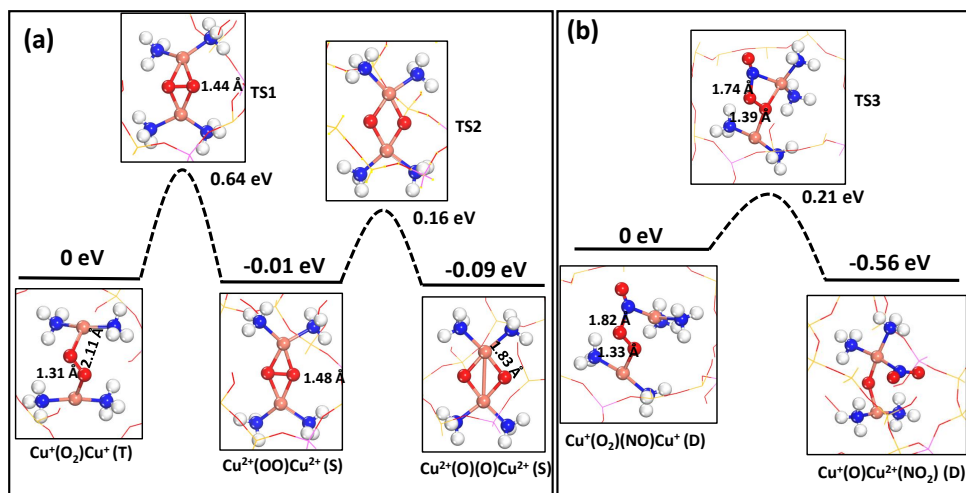


Figure 4.5: Dissociation of O<sub>2</sub> on a pair of complexes  $(\text{Cu}(\text{NH}_3)_x)^+$  in CHA. (a) Dissociation of O<sub>2</sub>, (b) Dissociation of O<sub>2</sub> in presence of NO. The reported energies are zero-point corrected. (S), (D) and (T) denote singlet, doublet and triplet state, respectively.

dissociation of O<sub>2</sub> over the pairs. Firstly, O<sub>2</sub> is adsorbed in a bridging position between two copper ions. Subsequently, the dissociation is a two step process with two barriers. The first barrier is 0.64 eV and involves the rotation of the molecule and the dissociation from the activated O<sub>2</sub> state proceeds with a small barrier of 0.16 eV barrier. As to the dissociated O<sub>2</sub> over the pairs, the two oxygen atoms are bonded between the two copper ions and the ligands are not linearly coordinated around the Cu-site anymore, which is a consequence of charge transfer and the formation of Cu(II). Figure 4.5(b) shows a path on activation of O<sub>2</sub> with the presence of NO. It is found that NO promotes O<sub>2</sub> dissociation and the NO-assisted path proceeds with a barrier of only 0.21 eV. The final state is a nitrite bonded on Cu together with one oxygen atom coordinated to both Cu ions.

Constrained molecular dynamics is employed to simulate the activation of oxygen on the Cu-complex pairs in CHA. The singlet state has been considered for this constrained MD simulation. The constraint in the MD is the linear combination of  $r_1$  and  $r_2$ . The  $r_1$  denotes the bond length between the lower Cu<sup>+</sup> ion and the left oxygen atom (shown in Figure 4.6) and the  $r_2$  denotes the bond length between the upper Cu<sup>+</sup> ion and the right oxygen atom (shown in Figure 4.6). The sum of  $r_1$  and  $r_2$  for the activated O<sub>2</sub> on the pairs is 3.89 Å and for the adsorbed O<sub>2</sub> on the pairs is 5.69 Å.

The free energy difference is analyzed by thermodynamic integration of free-energy gradients and is shown in Figure 4.6. A different path to activate oxygen was found during this MD simulation. A new intermediate structure is found and two barriers are overcome to activate oxygen on the Cu<sup>+</sup>-pairs in this path. In the new transition state (Figure 4.6), O<sub>2</sub> is activated on one Cu<sup>+</sup> ion with an stabilization by the other Cu<sup>+</sup>. This

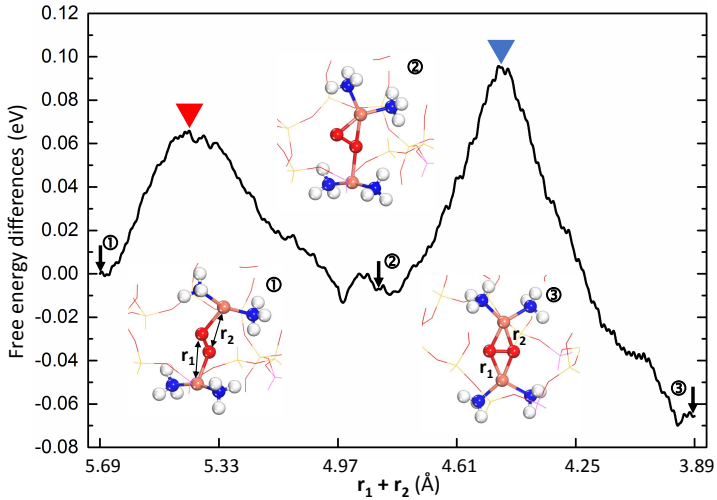


Figure 4.6: Free energy difference for activation of oxygen over a  $\text{Cu}^+$ -pair in Cu-CHA from constrained molecular dynamics. The structures in the insets marked with numbers are marked on the trajectory by arrows. The constrained MD simulation is performed on the singlet potential energy surface. Atom color codes: copper (orange), oxygen (red), nitrogen (blue), hydrogen (white), silicon (yellow), and aluminum (purple).

new path is very promising as the two barriers are much lower than the previous one (Figure 4.5). The barriers obtained from the MD was confirmed by NEB calculations.

For the NEB barrier calculation, singlet and triplet potential energy surfaces have been calculated to find the favorable spin states along the reaction path. For adsorbed  $\text{O}_2$  (see Figure 4.7), the triplet state is 0.25 eV lower than its singlet state and therefore the barriers is higher than that from the MD in Figure 4.6. The spin crossing appears before the first transition state. The second barrier from NEB is 0.14 eV, which is also close to the free energy barrier.

Noting that the Si to Al ratio is 5 when the  $\text{O}_2$  activation is investigated, the effect of a lower ratio on  $\text{O}_2$  activation is interesting to investigate. These calculations were done with SSZ-13 modelled using a hexagonal unit cell which has 36 Si atoms in tetrahedral (T) positions. In this large cell, two Si are replaced by two Al, which leads to a Si/Al ratio of 17. The detailed information on the two Al positions is included in Paper III. A similar constrained MD simulation is also performed to investigate the free energy barrier of  $\text{O}_2$  activation on the pairs. It is shown that the two barriers are very close to the barriers determined in the small CHA unit cell (Figure 4.6). Therefore, the Si to Al ratio seems have a minor effect on the  $\text{O}_2$  activation on the  $\text{Cu}^+$  pairs.

As soon as the  $\text{O}_2$  is activated with a bond length of 1.48 Å,  $\text{O}_2$  will be dissociated with a barrier of 0.28 eV. This step was also simulated from constrained MD and the free energy barrier is consistent with the NEB barrier.

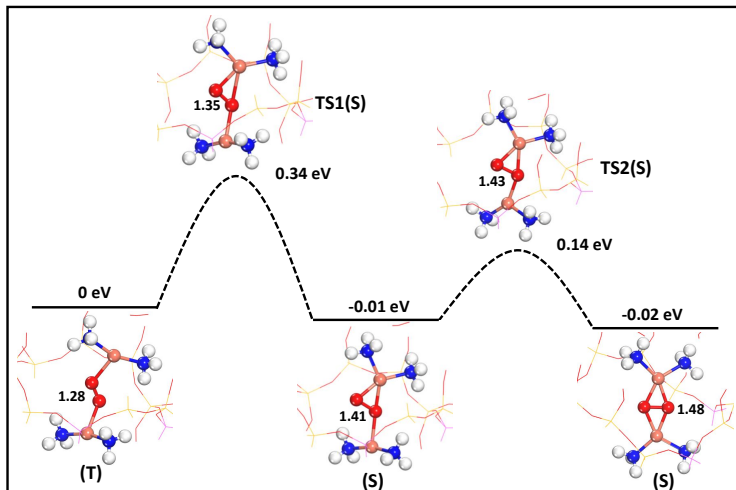


Figure 4.7: Path for activation of oxygen on the  $\text{Cu}^+$ -pairs in Cu-CHA from climbing image NEB calculations. The energies include zero-point energies. Atom color codes are same with Figure 4.6.

### 4.3 The effect of Al-distribution on $\text{Cu}^+$ -pairs formation

Since the activation of oxygen in  $\text{NH}_3$ -SCR over CHA involves the  $\text{Cu}(\text{NH}_3)_2^+$  pairs, it is of interest to know whether the formation of the  $\text{Cu}(\text{NH}_3)_2^+$  pair is affected by the Al distribution. In this part, the hexagonal CHA unit cell is used with two Si replaced by two Al, which gives the ratio of Si/Al 17. As the Al-sites can be assumed to be evenly distributed in the framework, all feasible configurations with two  $\text{Al}^{3+}$  in the hexagonal unit cell have been considered. Taking into account the structural symmetry and Lowenstein's rule (Al-O-Al links are forbidden), 52 different configurations are obtained. The detailed information on 52 configurations with site-labeling are listed in Paper III. Here 8 configurations (see green balls in Figure 4.8(b)) have been selected to calculate the  $\text{Cu}(\text{NH}_3)_2^+$ -pair formation energy according to:

$$\Delta E_{form} = E_{2\text{Cu}@CHA} + E_{\text{H}_2(gf)} - E_{2\text{H}@CHA} - E_{2\text{Cu}(gf)} \quad (4.1)$$

where  $E_{2\text{Cu}@CHA}$  is the total energy of the  $\text{Cu}(\text{NH}_3)_2^+$  pairs in the large cage,  $E_{2\text{H}@CHA}$  is the total energy of two protons in the CHA structure,  $E_{\text{H}_2(gf)}$  and  $E_{2\text{Cu}(gf)}$  are the total energy of hydrogen in gas phase and  $\text{Cu}(\text{NH}_3)_2^+$  pairs in gas phase, respectively. Here, molecular dynamics are performed at 400 k with 5 ps to sample the structures of the  $\text{Cu}(\text{NH}_3)_2^+$  pairs in the large cage of CHA.  $E_{2\text{Cu}@CHA}$  is calculated by geometry optimization of the structure with lowest energy along the MD trajectories.

The 8 configurations with a site-labeling are listed in Table 4.1. The 8 configurations have gradually increased Al-Al distance from the shortest 4.5 Å to the longest 13.77 Å. The Cu-Cu distances in the relaxed structure ranges from 3.32 Å to 5.32 Å. From previous calculations, it is known that the Cu-Cu distance is at least  $\sim 5.0$  Å to be able to adsorb

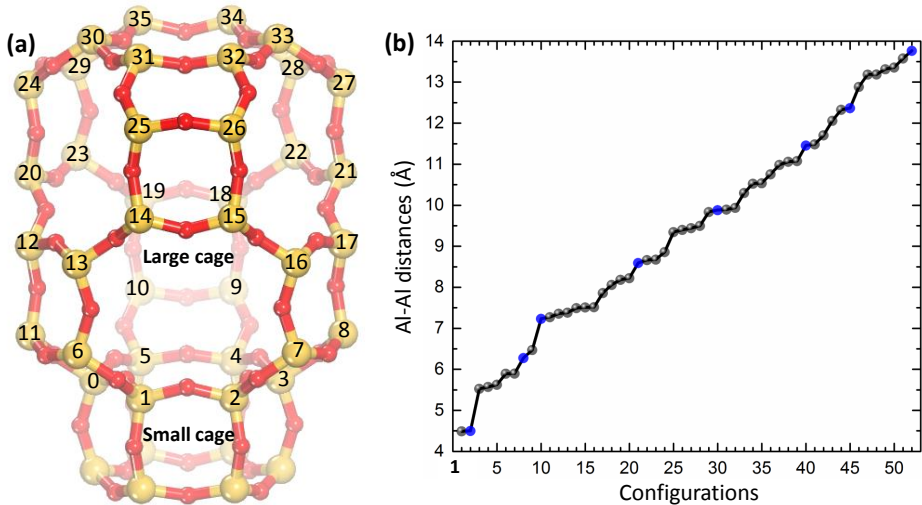


Figure 4.8: (a) The large and small cavity of CHA structure and the large cavity is completely build up by a hexagonal CHA unit cell. All Si atoms are marked with numbers to make the following statement easier on the replaced Al sites. (b) Al-Al distance with respect to the 52 configurations with 2 Al replacing two Si in the (a) structure. The blue balls represent the configurations are chosen to investigate the effect of Al-distribution on  $\text{Cu}^+$ -pairs formation.

$\text{O}_2$  between the  $\text{Cu}(\text{NH}_3)_2^+$  pairs.

Conf.	Site labels	Al-Al distance (Å)	Cu-Cu distance (Å)
1	0 + 6	4.50	3.32
2	0 + 3	6.28	5.05
3	0 + 20	7.24	4.7
4	0 + 18	8.60	5.32
5	0 + 15	9.88	4.76
6	11 + 26	11.46	4.91
7	0 + 31	12.37	5.29
8	11 + 27	13.77	4.85

Table 4.1: The 8 configurations where two  $\text{Si}^{4+}$  are replaced by  $\text{Al}^{3+}$ . The site labels refer to the numbering in Figure 4.8(a). Cu-Cu distance is measured for the pairs in the large cage of CHA, which is relaxed structure from MD trajectories.

The results for the stability of pairs and protons are shown in Figure 4.9. The Al-distribution has a negligible effect on the stability of the protons as the relative energies are within 0.1 eV (dark gray line with square symbols). Regarding the relative formation energies of the  $\text{Cu}(\text{NH}_3)_2^+$  pairs in CHA (green line with circle symbols), we find a difference in stability of about 0.55 eV for the considered structures. Configuration 3

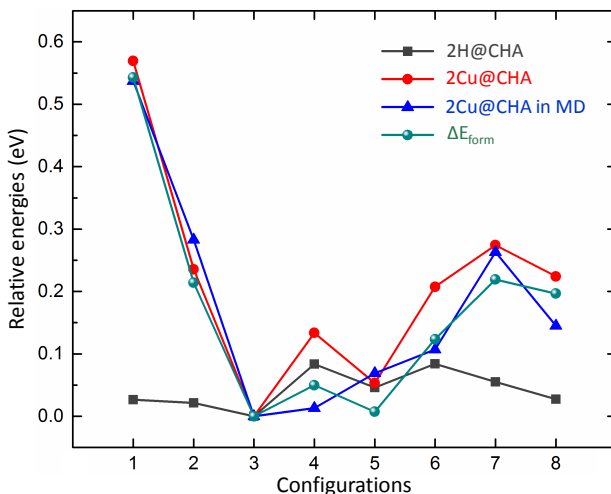


Figure 4.9: Relative energies of the 8 configuration numbers. The dark gray line with square symbols represent the total energies of two protons as Lewis acid sites in SSZ-13. The red line with circle symbols stand the total energies of the  $\text{Cu}(\text{NH}_3)_2^+$  pairs in the CHA large cage. The blue line with triangle symbols show the average ground state energies of the pairs in the CHA large cage from MD simulations. The green line with ball symbols are the pair-formation energies for the 8 configurations. All the energies are showing with respect to the corresponding energy of configuration 3.

has the highest stability among the 8 configurations, whereas configuration 1 has the lowest stability. The other configurations (2, 6, 7 and 8) have similar stability (within 0.1 eV) but clearly not as stable as configurations 3, 4 and 5. Thus, we conclude that an Al-distribution such as configuration 1 yields a probability for the  $\text{Cu}(\text{NH}_3)_2^+$  pair formation considerably lower than, for example, configuration 3.

In order to investigate possible entropic contributions to the relative stability, the time average of the potential energies along the trajectories are also reported in Figure 4.9 (blue line). The MD results show that, again, configuration 3 has the highest stability and configuration 1 has the lowest stability. The average total potential energies for configuration 2 and 7 show that they are less stable than configuration 3 by  $\sim 0.3$  eV. Configuration 4, 5 and 6 almost have the same stability with configuration 3 and the average total potential energy difference is within 0.1 eV. The average total potential energy for configuration 8 is  $\sim 0.15$  eV higher than that of configuration 3. The AIMD results support the static calculations that the stability of the pairs in the CHA large cage is sensitive to the Al-distribution. As the activation of  $\text{O}_2$  in  $\text{NH}_3$ -SCR involves the  $\text{Cu}(\text{NH}_3)_2^+$  pairs, the Al-distribution will affect the activation of  $\text{O}_2$ .

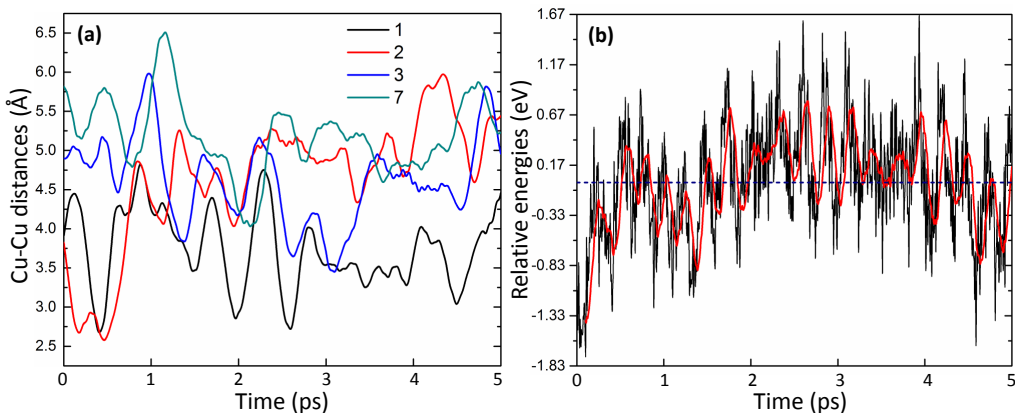


Figure 4.10: (a) Cu-Cu distances between the  $\text{Cu}(\text{NH}_3)_2^+$  pairs along the AIMD trajectories for configurations 1, 2, 3 and 7 in table 4.1. (b) The potential energies of the pairs in configuration 3 along the AIMD trajectories. The energies are relative to the average relative potential energy for the entire AIMD trajectories, which is shown as dash line. The red line is the moving averages of the relative potential energies calculated by every 0.1 ps with 0.05 ps intervals.

#### 4.4 The dynamic character of Cu sites in CHA

It is also of interest to study the Cu-Cu distances during the MD simulations for the 8 configurations. Figure 4.10(a) shows the Cu-Cu distances between the  $\text{Cu}(\text{NH}_3)_2^+$  pairs along the MD trajectories for configurations 1,2,3 and 7. The Cu-Cu distances in configuration 1 have a range from  $\sim 2.5$  Å to  $\sim 5$  Å. The configuration 2 has slightly larger range of the Cu-Cu distances within  $\sim 2.5$ - $\sim 6$  Å. The configurations 3 and 7 have longer Cu-Cu distances along the MD simulation than the configuration 1. This may explain the lower stability of the  $\text{Cu}(\text{NH}_3)_2^+$  pairs in the case of configuration 1. In Figure 4.10(b), the potential energies of the pairs in configuration 3 along the AIMD trajectories are shown. The moving averages of the potential energies indicates the stability of the pairs in this case is effected by the Cu-Cu distance.

To investigate the dynamic character of the  $\text{Cu}(\text{NH}_3)_2^+$  complex crossing the eight membered ring in CHA framework, a longer MD with 15 ps has been simulated at 473 K in the 2x1 CHA rhombohedral cell. Two Si are replaced by two Al, which gives the Si/Al ratio of 11. To maintain the charge neutrality for this system, a proton is bonded with one oxygen atom near one Al as a Lewis acid site. By analyzing the trajectories, the N-Cu-N angles are varying along the MD simulation, which is shown in the left panel of Figure 4.11. The right panel of Figure 4.11 shows the trajectories of Cu ion in the 2x1 CHA rhombohedral cell. During the simulation, the  $\text{Cu}(\text{NH}_3)_2^+$  complex crosses the eight-membered ring. When the complex is crossing the ring, the structural properties of the complex have been changed. The structure of the complex when it crosses the ring is shown in the left panel of Figure 4.11. It is interesting to see that the complex has changed its shape to a bent coordination. The complex is almost linear before and after

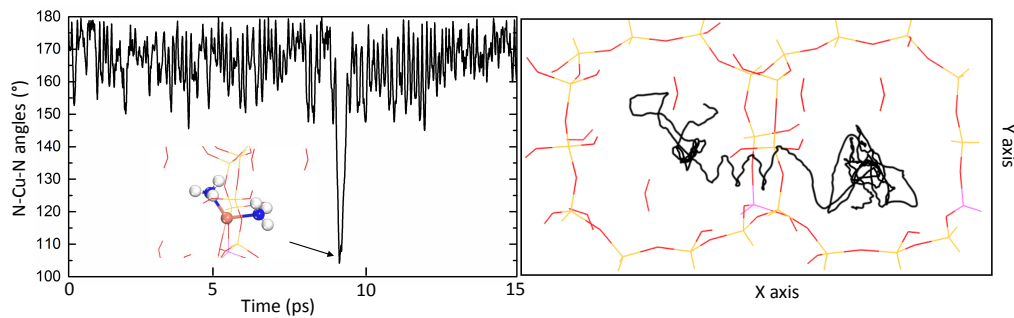


Figure 4.11: A 15 ps MD simulation for a  $\text{Cu}(\text{NH}_3)_2^+$  complex in 2x1 CHA rhombohedral cell. The left panel is N-Cu-N angles along the MD trajectories and the right panel is the moving trajectory of Cu ion in the 2x1 cell. The arrow in the left panel shows the structure with the smallest angle of N-Cu-N along the simulation.

its crossing the ring. It can be concluded that the  $\text{Cu}(\text{NH}_3)_2^+$  complex in CHA is very dynamic under the operating temperature regarding both its position in CHA and its geometric shape.

# Chapter 5

## Conclusion and outlook

The aim of this thesis has mainly been to study the character of  $\text{Cu}^+$  ions during the solid-state ion-exchange process and activation of oxygen during  $\text{NH}_3$ -SCR in Cu-CHA. This has been performed by electronic structure calculations in combination with *ab-initio* thermodynamics and molecular dynamics. To compare with the experimental results, activation energies, thermodynamic phase diagram as well as vibrational frequencies have been calculated.

The energetic conditions for functionalization of CHA with copper ions in SSIE from  $\text{Cu}_2\text{O}(111)$  via the formation of  $\text{Cu}(\text{NH}_3)_2^+$  have been investigated. The study shows that the diamine complexes form easily on  $\text{Cu}_2\text{O}(111)$  and diffuse with low barriers over the surface and in the CHA framework. The charge neutrality of the systems is maintained via counterdiffusion of  $\text{H}^+$  in the form of  $\text{NH}_4^+$  from the zeolite to the  $\text{Cu}_2\text{O}$  surface where water can be formed. The efficient solvation of  $\text{Cu}^+$  and  $\text{H}^+$  by ammonia renders the ion-exchange process exothermic. In this study, the dynamic of character of Cu ion sites in CHA in the presence of ammonia is highlighted.

The activation of oxygen, one crucial step during  $\text{NH}_3$ -SCR reactions, is investigated in detail. The understanding of this reaction step is coupled to the understanding of the active site during reaction conditions. Under SCR-conditions,  $\text{Cu}(\text{NH}_3)_2^+$  is the preferable species at temperature below  $\sim 523$  K. Direct dissociation of  $\text{O}_2$  is found to be facile over a pair of  $\text{Cu}(\text{NH}_3)_2^+$  whereas dissociation on a single  $\text{Cu}(\text{NH}_3)_2^+$  species is unlikely due to a high activation energy. When the temperature is above  $\sim 623$  K, copper sites are preferably framework-coordinated without any ligands solvated. In this case, the  $\text{NH}_3$ -SCR catalytic cycle is able to be fulfilled over the framework-coordinated Cu sites in CHA. The character of active sites during  $\text{NH}_3$ -SCR is consequently very condition-dependent, where the low temperature reaction occurs on Cu-solvated species and the high temperature reaction occurs on framework-coordinated Cu sites. These two kinetic regimes link homo- and heterogeneous catalysis.

Given that the  $\text{Cu}(\text{NH}_3)_2^+$  pairs are required for direct  $\text{O}_2$  activation and dissociation for  $\text{NH}_3$ -SCR in zeolites, the effect of Al distribution on the stability of the pair formation in CHA are further investigated. The Al distribution is found to strongly affect the propensity to form the  $\text{Cu}(\text{NH}_3)_2^+$  pairs in CHA. In particular, the difference in pair “formation” energies as a function of Al-distribution is relative high. The results indicate that precise synthesis of Cu exchanged CHA with respect to Al distribution may enable enhance the catalytic activity.

In the present work, we have not evaluated the barriers for the side reactions in  $\text{NH}_3$ -SCR, such as  $\text{NH}_3$  oxidation or  $\text{N}_2\text{O}$  formation. Therefore, we would like to look into this in the future.



# Acknowledgments

The research work in this thesis was carried out at the Division of Chemical Physics at the Department of Physics and the Competence Centre for Catalysis (KCK) at Chalmers University of Technology, Göteborg, Sweden, from August 2015 to November 2017.

This research is financially supported by the Swedish Energy Agency and the member companies AB Volvo, ECAPS AB, Haldor Topsøe A/S, Scania CV AB, Volvo Car Corporation AB, and Wärtsilä Finland Oy. Additional financial support from the Swedish Research Council and the Chalmers Area of Advance Transport is acknowledged. The calculations have been performed at C3SE (Göteborg) and PDC (Stockholm) through a SNIC grant.

Additionally, I would like to express my sincere gratitude to:

My main supervisor, Henrik Grönbeck, for your patience, motivation, enthusiasm, and immense knowledge. I benefit greatly from the many fruitful discussions with you. Your positive outlook to science always inspires me. It is of a great pleasure to work with you.

My co-supervisors, Magnus Skoglundh and Anders Hellman, for your constant support of my project. Magnus, thanks for your insightful ideas on our project meetings. Anders, thanks for your advices on my thesis.

My collaborators, Jonas Jansson, Hanne Falsig and Ton V.W. Janssens. Jonas, thanks for every discussion we have had. Your advice truly improves our research. Hanne and Ton, thanks for your participation in our project. It is really joyful to have our regular skype meetings with you. I have learnt a lot from your insightful ideas from both theoretical and experimental perspective.

All my colleagues at Chemical Physics for creating a friendly working environment. In particular, I would like to give thanks to our theoretical people Adam, Alvaro, Baochang, Lucy, Matej, Matthias, Maxime, Michael, Mikael, Mikkell, and Unni. I also would like to thank the experimental people Aadesh, Arturo, Ligang, Sara, Su and all others. Thanks to our 'pingpong' team for playing pingpong every now and then.

All KCK members for your sharing results and ideas. Thank you!

My friends here for all your support and having fun together. Especially thanks to Daixin, Linr, Linlin, Qi, Wanying, Xianchan, Gaowa, Ren and all others.

Last but not least, I want to thank my parents and Qing for your endless support and love throughout my life, without which I would not have come this far.



# Bibliography

- [1] C. Adams. Applied Catalysis: A Predictive Socioeconomic History. *Top. Catal.*, 52: 924–934, 2009.
- [2] J. K. Smith. *History of Catalysis*. John Wiley & Sons, 2010. ISBN 9780471227618.
- [3] H. S. Taylor. The Heterogeneity of Catalyst Surfaces for Chemisorption. *Adv. Catal.*, 1:1–26, 1948.
- [4] Jeffrey P. Greeley. Active Site of an Industrial Catalyst. *Science*, 336:810–811, 2012.
- [5] J. M. Thomas, R. Raja, and D. W. Lewis. Single-Site Heterogeneous Catalysts. *Angew. Chem. Int. Ed.*, 44:6456–6482, 2005.
- [6] J. M. Thomas and R. Raja. The Advantages and Future Potential of Single-Site Heterogeneous Catalysts. *Top. Catal.*, 40:3–17, 2006.
- [7] J. M. Thomas. *Design and Applications of Single-Site Heterogeneous Catalysts*. Imperial College Press, 2012. ISBN 978-1-84816-909-8.
- [8] S. Back, J. Lim, N.Y. Kim, Y.H. Kimb, and Y. Jung. Single-Atom Catalysts for CO<sub>2</sub> Electroreduction with Significant Activity and Selectivity Improvements. *Chem. Sci.*, 8:1090–1096, 2017.
- [9] G. Vilé, D. Albani, M. Nachtegaal, Z. Chen, D. Dontsova, M. Antonietti, N. López, and J. Pérez-Ramírez. A Stable Single-Site Palladium Catalyst for Hydrogenations. *Angew. Chem. Int. Ed.*, 54:11265–11269, 2015.
- [10] D.G.H. Ballard. Pi and Sigma Transition Metal Carbon Compounds as Catalysts for the Polymerization of Vinyl Monomers and Olefins. *Adv. Catal.*, 23:263–325, 1973.
- [11] B. M. Lok, C. A. Messina, R. L. Patton, R. T. Gajek, T. R. Cannan, and E. M. Flanigen. Silicoaluminophosphate Molecular Sieves: Another New Class of Microporous Crystalline Inorganic Solids. *J. Am. Chem. Soc.*, 106:6092–6093, 1984.
- [12] C. Doblin, J. F. Mathews, and T. W. Turney. Shape Selective Cracking Ofn-octane and 2,2,4-trimethylpentane over an Alumina-Pillared Clay. *J. Am. Chem. Soc.*, 23: 151–160, 1994.
- [13] V. D. Santo, F. Liguori, C. Pirovano, and M. Guidotti. Design and Use of Nanostructured Single-Site Heterogeneous Catalysts for the Selective Transformation of Fine Chemicals. *Molecules*, 15:3829–3856, 2010.
- [14] J.H. Kwak, J.H. Lee, S.D. Burton, A.S. Lipton, C.H. Peden, and J. Szanyi. A Common Intermediate for N<sub>2</sub> Formation in Enzymes and Zeolites: Side-On Cu–Nitrosyl Complexes. *Angew. Chem. Int. Ed.*, 52:9985–9989, 2013.

- [15] D. W. Fickel and R. F. Lobo. Copper Coordination in Cu-SSZ-13 and Cu-SSZ-16 Investigated by Variable-Temperature XRD. *J. Phys. Chem. C*, 114:1633–1640, 2010.
- [16] M.H. Mahyuddin, A. Staykov, Y. Shiota, and K. Yoshizawa. Direct Conversion of Methane to Methanol by Metal-Exchanged ZSM-5 Zeolite (Metal = Fe, Co, Ni, Cu). *ACS Catal.*, 6:8321–8331, 2016.
- [17] B. Qi, X.H. Lu, D. Zhou, Q.H. Xia, Z.R. Tang, S.Y. Fang, T.Pang, and Y.L. Dong. Catalytic Epoxidation of Alkenes with 30% H<sub>2</sub>O<sub>2</sub> over Mn<sup>2+</sup>-Exchanged Zeolites. *J. Mol. Catal. A: Chem.*, 322:73–79, 2010.
- [18] A. Kubacka, E. Włoch, B. Sulikowski, R.X Valenzuela, and V.C. Corberán. Oxidative Dehydrogenation of Propane on Zeolite Catalysts. *Catal. Today*, 61:343–352, 2000.
- [19] D. Jo, T. Ryu, G.T. Park, P.S. Kim, C. H. Kim, I. Nam, and S.B. Hong. Synthesis of High-Silica LTA and UFI Zeolites and NH<sub>3</sub>-SCR Performance of Their Copper-Exchanged Form. *ACS Catal.*, 6:2443–2447, 2016.
- [20] S. Brandenberger, O. Kröcher, A. Tissler, and R. Althoff. The State of the Art in Selective Catalytic Reduction of NO<sub>x</sub> by Ammonia Using Metal-Exchanged Zeolite Catalysts. *Cat. Rev. - Sci. Eng.*, 50:492–531, 2008.
- [21] P. Tomkins, M. Ranocchiari, and J. A. van Bokhoven. Direct Conversion of Methane to Methanol under Mild Conditions over Cu-Zeolites and Beyond. *Acc. Chem. Res.*, 50:418–425, 2017.
- [22] P.L.T. Gabrielsson. Urea-SCR in Automotive Applications. *Top. Catal.*, 28:177–184, 2004.
- [23] T. Kobayashi, T.Yamada, and K.Kayano. Effect of Basic Metal Additives on NO<sub>x</sub> Reduction Property of Pd-based Three-way Catalyst. *Appl. Catal., B*, 30:287–292, 2001.
- [24] L. Lietti, P. Forzatti, I. Nova, and E. Tronconi. NO<sub>x</sub> Storage Reduction over Pt-Ba/γ-Al<sub>2</sub>O<sub>3</sub> Catalyst. *J. Catal.*, 204:175–191, 2001.
- [25] J.H. Kwak, H. Zhu, J.H. Lee, C.H. Peden, and J. Szanyi. Two Different Cationic Positions in Cu-SSZ-13? *Chem. Commun.*, 48:4758–4760, 2012.
- [26] F. Gao, J. H. Kwak, J. Szanyi, and C. H. Peden. Current Understanding of Cu-Exchanged Chabazite Molecular Sieves for Use as Commercial Diesel Engine DeNO<sub>x</sub> Catalysts. *Acc. Chem. Res.*, 56:1441–1459, 2013.
- [27] M. Koebel, M. Elsener, and M. Kleemann. Urea-SCR: A Promising Technique to Reduce NO<sub>x</sub> Emissions from Automotive Diesel Engines. *Catal. Today*, 59:335–345, 2000.

- [28] T. Shikada, K. Fujimoto, T. Kunugi, H. Tominaga, S. Kaneko, and Y. Kubo. Reduction of Nitric Oxide with Ammonia on Vanadium Oxide Catalysts Supported on Homogeneously Precipitated Silica-Titania. *Ind. Eng. Chem. Prod. Res. Dev.*, 20:91–95, 1981.
- [29] V.I. Pârvulescua, P. Grangeb, and B. Delmonb. Catalytic Removal of NO. *Catal. Today*, 46:233–316, 1998.
- [30] A. M. Frey, S. Mert, J. Due-Hansen, R. Fehrmann, and C.H. Christensen. Fe-BEA Zeolite Catalysts for NH<sub>3</sub>-SCR of NO<sub>x</sub>. *Catal. Lett.*, 130:1–8, 2009.
- [31] T. V. W. Janssens, H. Falsig, L. F. Lundegaard, P. N. R. Vennestrøm, S. B. Rasmussen, P. G. Moses, F. Giordanino, E. Borfecchia, K. A. Lomachenko, C. Lamberti, and S. Bordiga. A Consistent Reaction Scheme for the Selective Catalytic Reduction of Nitrogen Oxides with Ammonia. *ACS Catal.*, 5:2832–2845, 2015.
- [32] F. Giordanino, E. Borfecchia, K. A. Lomachenko, A. Lazzarini, G. Agostini, E. Gallo, A. V. Soldatov, P. Beato, S. Bordiga, and C. Lamberti. Interaction of NH<sub>3</sub> with Cu-SSZ-13 Catalyst: A Complementary FTIR, XANES, and XES Study. *J. Phys. Chem. Lett.*, 5:1552–1559, 2014.
- [33] A. Godiksen, F. N. Stappen, P. N. R. Vennestrøm, F. Giordanino, S. B. Rasmussen, L. F. Lundegaard, and S. Mossin. Coordination Environment of Copper Sites in Cu-CHA Zeolite Investigated by Electron Paramagnetic Resonance. *J. Phys. Chem. C*, 118:17207–17212, 2014.
- [34] Werner Heisenberg and Paul Davies. *Physics and Philosophy: The Revolution in Modern Science*. Penguin, 2000. ISBN 0141182156, 9780141182155.
- [35] F. Jensen. *Introduction to Computational Chemistry*. John Wiley & Sons Inc, 2007. ISBN 0470011874, 978-0470011874.
- [36] R. M. Martin. *Electronic Structure: Basic Theory and Practical Methods*. Cambridge University Press, 2008. ISBN 0521534402, 978-0521534406.
- [37] Werner Heisenberg. Über den Anschaulichen Inhalt der Quantentheoretischen Kinematik und Mechanik. *Zeitschrift für Physik*, 43:172–198, 1927.
- [38] E. Schrödinger. Quantisierung Als Eigenwertproblem. *Annalen der Physik*, 385: 437–490, 1926.
- [39] W. Koch and M.C. Holthausen. *A Chemist’s Guide to Density Functional Theory*. Wiley-VCH, 2001. ISBN 978-3-527-30372-4.
- [40] S.T. Epstein. *The Variation Method in Quantum Chemistry*. Academic Press, 1974. ISBN 0122405501.
- [41] M. Born and R. Oppenheimer. Zur quantentheorie der molekeln. *Ann. Phys.*, 389: 457–484, 1927.

- [42] C.F. Fischer. *The Hartree-Fock Method for Atoms: A Numerical Approach*. John Wiley & Sons, 1977. ISBN 047125990X, 978-0471259909.
- [43] L.H. Thomas. The Calculation of Atomic Fields. *Proc. Cambridge. Phil. Soc.*, 23: 542–548, 1927.
- [44] Enrico Fermi. Un Metodo Statistico per la Determinazione di alcune Proprietà dell'Atomo. *Rend. Accad. Naz. Lincei.*, 6:602–607, 1927.
- [45] P. A. M. Dirac. Note on Exchange Phenomena in the Thomas Atom. *Proc. Cambridge. Phil. Soc.*, 26:376–385, 1930.
- [46] Edward Teller. On the Stability of Molecules in the Thomas-Fermi Theory. *Rev. Mod. Phys.*, 34:627–631, 1962.
- [47] P. Hohenberg and W. Kohn. Inhomogeneous Electron Gas. *Phys. Rev.*, 136: B864–B871, 1964.
- [48] W. Kohn and L. J. Sham. Self-Consistent Equations Including Exchange and Correlation Effects. *Phys. Rev.*, 140:A1133–A1138, 1965.
- [49] R. O. Jones and O. Gunnarsson. The Density Functional Formalism, Its Applications and Prospects. *Rev. Mod. Phys.*, 689:689–746, 1989.
- [50] F. Herman, J. P. Van Dyke, and I. B. Ortenburger. Improved Statistical Exchange Approximation for Inhomogeneous Many-Electron Systems. *Phys. Rev. Lett.*, 22: 807–811, 1969.
- [51] R. A. Evarestov. *Quantum Chemistry of Solids*. Springer, 2007. ISBN 978-3-642-08022-7.
- [52] John P. Perdew and Wang Yue. Accurate and Simple Density Functional for the Electronic Exchange Energy: Generalized Gradient Approximation. *Phys. Rev. B*, 33:8800–8822, 1986.
- [53] John P. Perdew, J. A. Chevary, S. H. Vosko, Koblak A. Jackson, Mark R. Pederson, D. J. Singh, and Carlos Fiolhais. Atoms, Molecules, Solids, and Surfaces: Applications of the Generalized Gradient Approximation for Exchange and Correlation. *Phys. Rev. B*, 46:6671–6687, 1992.
- [54] John P. Perdew, Kieron Burke, and Matthias Ernzerhof. Generalized Gradient Approximation Made Simple. *Phys. Rev. Lett.*, 77:3865–3868, 1996.
- [55] A. D. Becke. Density-Functional Exchange-Energy Approximation with Correct Asymptotic Behavior. *Phys. Rev. A*, 38:3098–3100, 1988.
- [56] L. Chen, J. Jansson, M. Skoglundh, and H. Grönbeck. Mechanism for Solid-State Ion Exchange of  $\text{Cu}^+$  into Zeolites. *J. Phys. Chem. C*, 120:29182–29189, 2016.
- [57] A. D. Becke. A New Mixing of Hartree-Fock and Local Density-Functional Theories. *J. Chem. Phys.*, 98:1372–1377, 1993.

- [58] Chengteh Lee, Weitao Yang, and Robert G. Parr. Development of the Colle-Salvetti Correlation-Energy Formula into a Functional of the Electron Density. *Phys. Rev. B*, 37:785–789, 1988.
- [59] C. Adamo and B. Vincenzo. Toward Reliable Density Functional Methods without Adjustable Parameters: The PBE0 Model. *J. Chem. Phys.*, 110:6158–6170, 1999.
- [60] J. Heyd and G. E. Scuseria. Hybrid Functionals Based on a Screened Coulomb Potential. *J. Chem. Phys.*, 118:8207–8215, 2003.
- [61] J. Wellendorff, K. T. Lundgaard, A. Møgelhøj, V. Petzold, D. D. Landis, J. K. Nørskov, T. Bligaard, and K. W. Jacobsen. Higher-Accuracy Van Der Waals Density Functional. *Phys. Rev. B*, 85:235149, 2012.
- [62] K. Lee, É. D. Murray, L. Kong, B. I. Lundqvist, and D. C. Langreth. Higher-Accuracy Van Der Waals Density Functional. *Phys. Rev. B*, 82:8207–8215, 2010.
- [63] P. E. Blöchl. Projector Augmented-Wave Method. *Phys. Rev. B*, 50:17953–17979, 1994.
- [64] G. Kresse and D. Joubert. From Ultrasoft Pseudopotentials to the Projector Augmented-Wave Method. *Phys. Rev. B*, 59:1758–1775, 1999.
- [65] J. M. Thomas and W. J. Thomas. *Principles and Practice of Heterogeneous Catalysis*. Wiley VCH, 1996. ISBN 978-3527292394.
- [66] H. Öström, H. Öberg, H. Xin, J. LaRue, M. Beye, M. Dell’Angela, J. Gladh, M. L. Ng, J. A. Sellberg, S. Kaya, G. Mercurio, D. Nordlund, M. Hantschmann, F. Hieke, D. Kühn, W. F. Schlotter, G. L. Dakovski, J. J. Turner, M. P. Minitti, A. Mitra, S. P. Moeller, A. Föhlich, M. Wolf, W. Wurth, M. Persson, J. K. Nørskov, F. Abild-Pedersen, H. Ogasawara, L. G. M. Pettersson, and A. Nilsson. Probing the Transition State Region in Catalytic CO Oxidation on Ru. *Science*, 347:978–982, 2015.
- [67] M. R. Hestenes and E. Stiefel. Methods of Conjugate Gradients for Solving Linear Systems. *Journal of Research of the National Bureau of Standards*, 49:409–436, 1952.
- [68] G. Kresse and J. Hafner. Ab Initio Molecular Dynamics for Open-Shell Transition Metals. *Phys. Rev. B*, 48:13115–13118, 1993.
- [69] G. Kresse and J. Hafner. Ab Initio Molecular-Dynamics Simulation of the Liquid-Metal–Amorphous-Semiconductor Transition in Germanium. *Phys. Rev. B*, 49:14251–14269, 1994.
- [70] K. Reuter and M. Scheffler. Composition, Structure, and Stability of RuO<sub>2</sub>(110) as a Function of Oxygen Pressure. *Phys. Rev. B*, 65:035406, 2001.
- [71] M. Scheffler. Thermodynamic Aspects of Bulk and Surface Defects - First-Principle Calculations -. *Stud. Surf. Sci. Catal.*, 40:115–122, 1988.

- [72] Stanley I. Sandler. *An Introduction to Applied Statistical Thermodynamics*. Wiley, 2010. ISBN 0470913479, 978-0470913475.
- [73] G. Mills, H. Jónsson, and G. K. Schenter. Reversible Work Transition State Theory: Application to Dissociative Adsorption of Hydrogen. *Surf. Sci.*, 324:305–337, 1995.
- [74] G. Henkelman and H. Jónsson. Improved Tangent Estimate in the Nudged Elastic Band Method for Finding Minimum Energy Paths and Saddle Points. *J. Chem. Phys.*, 113:9978–9985, 2000.
- [75] G. Henkelman and H. Jónsson. A Dimer Method for Finding Saddle Points on High Dimensional Potential Surfaces Using Only First Derivatives. *J. Chem. Phys.*, 111:7010–7022, 1999.
- [76] G. Henkelman, B. P. Uberuaga, and H. Jónsson. A Climbing Image Nudged Elastic Band Method for Finding Saddle Points and Minimum Energy Paths. *J. Chem. Phys.*, 113:9901–9904, 2000.
- [77] D. Frenkel and B. Smit. *Understanding Molecular Simulation*. Academic, 2002. ISBN 978-0-12-267351-1.
- [78] R. N. Barnett, U. Landman, A. Nitzan, and G. Rajagopal. Born–Oppenheimer Dynamics Using Density-Functional Theory: Equilibrium and Fragmentation of Small Sodium Clusters. *J. Chem. Phys.*, 94:608–616, 1991.
- [79] R. Car and M. Parrinello. Unified Approach for Molecular Dynamics and Density-Functional Theory. *Phys. Rev. Lett.*, 55:2471–2474, 1985.
- [80] W. C. Swope and H. C. Andersen. A Computer Simulation Method for the Calculation of Equilibrium Constants for the Formation of Physical Clusters of Molecules: Application to Small Water Clusters. *J. Chem. Phys.*, 76:637–649, 1982.
- [81] S. Nosé. A Unified Formulation of the Constant Temperature Molecular Dynamics Methods. *J. Chem. Phys.*, 81:511–519, 1984.
- [82] S. Nosé. A Molecular Dynamics Method for Simulations in the Canonical Ensemble. *Mol. Phys.*, 52:255–268, 1984.
- [83] W. G. Hoover. Canonical Dynamics: Equilibrium Phase-Space Distributions. *Phys. Rev. A*, 31:1695–1697, 1985.
- [84] M. Sprik. Free Energy from Constrained Molecular Dynamics. *J. Chem. Phys.*, 109:7737–7744, 1998.
- [85] E. A. Carter, G. Ciccotti, J. T. Hynes, and R. Kapral. Constrained Reaction Coordinate Dynamics for the Simulation of Rare Events. *Chem. Phys. Lett.*, 156:472–477, 1989.
- [86] J. P. Ryckaert, G. Ciccotti, and H. J. C. Berendsen. Numerical Integration of the Cartesian Equations of Motion of a System with Constraints: Molecular Dynamics of N-Alkanes. *J. Comp. Phys.*, 23:327–341, 1977.

- [87] E. Darve, M. A. Wilson, and A. Pohorille. Calculating Free Energies Using a Scaled-Force Molecular Dynamics Algorithm. *Mol. Simul.*, 28:113–144, 2002.
- [88] W. K. Den Otter and W. J. Briels. Free Energy from Molecular Dynamics with Multiple Constraints. *Mol. Phys.*, 98:773–781, 2000.
- [89] P. Fleurat-Lessard and T. Ziegler. Tracing the Minimum-Energy Path on the Free-Energy Surface. *J. Chem. Phys.*, 123:084101, 2005.
- [90] T. Bucko. Ab Initio Calculations of Free-Energy Reaction Barriers. *J. Phys. Condens. Matt*, 20:064211, 2008.
- [91] C. Paolucci, A. A. Parekh, I. Khurana, J. R. Di Iorio, H. Li, J. D. Albarracin Caballero, A. Shih, T. Anggara, W. N. Delgass, J. T. Miller, and F. H. Ribeiro. Catalysis in a Cage: Condition-Dependent Speciation and Dynamics of Exchanged Cu Cations in SSZ-13 Zeolites. *J. Am. Chem. Soc.*, 138:6028–6048, 2016.
- [92] J. H. Kwak, D. Tran, J. Szanyi, C. H. Peden, and J. H. Lee. The Effect of Copper Loading on the Selective Catalytic Reduction of Nitric Oxide by Ammonia over Cu-SSZ-13. *Catal. Lett.*, 142:295–301, 2012.
- [93] K. A. Lomachenko, E. Borfecchia, C. Negri, G. Berlier, C. Lamberti, P. Beato, H. Falsig, and S. Bordiga. The Cu-CHA deNO<sub>x</sub> Catalyst in Action: Temperature-Dependent NH<sub>3</sub>-Assisted Selective Catalytic Reduction Monitored by Operando XAS and XES. *J. Am. Chem. Soc.*, 138:12025–12028, 2016.
- [94] A. K. S. Clemens, A. Shishkin, P.-A. Carlsson, M. Skoglundh, Z. Matěj F. J. Martínez-Casado, O. Balmes, and H. Härelind. Reaction-Driven Ion Exchange of Copper into Zeolite SSZ-13. *ACS Catal.*, 5:6209–6218, 2015.
- [95] J. H. Kwak, R. G. Tonkyn, D. H. Kim, J. Szanyi, and C. H. Peden. Excellent Activity and Selectivity of Cu-SSZ-13 in the Selective Catalytic Reduction of NO<sub>x</sub> with NH<sub>3</sub>. *J. Catal.*, 275:187–190, 2010.
- [96] A. M. Beale, F. Gao, I. Lezcano-Gonzalez, C. H. Peden, and J. Szanyi. Recent Advances in Automotive Catalysis for NO<sub>x</sub> Emission Control by Small-Pore Microporous Materials. *Chem. Soc. Rev.*, 44:7371–7405, 2015.
- [97] A. Clearfield. Crystal Structure of Chabazite, A Molecular Sieve. *Chem. Rev.*, 88:125–148, 1988.
- [98] E. Kikuchi, M. Ogura, I. Terasaki, and Y. Goto. Selective Reduction of Nitric Oxide with Methane on Gallium and Indium Containing H-ZSM-5 Catalysts: Formation of Active Sites by Solid-State Ion Exchange. *J. Catal.*, 161:1794–1796, 1996.
- [99] M. Zamadics, X.H. Chen, and L. Kevan. Solid-State Ion Exchange in H-SAPO-34: Electron Spin Resonance and Electron Spin Echo Modulation Studies of Copper (II) Location and Adsorbate Interaction. *J. Phys. Chem.*, 96:5488–5491, 1992.

- [100] F. Gao, E. D. Walter, N. M. Washton, J. Szanyi, and C. H. Peden. Synthesis and Evaluation of Cu/SAPO-34 Catalysts for NH<sub>3</sub>-SCR 2: Solid-State Ion Exchange and One-Pot Synthesis. *Appl. Catal., B*, 162:501–514, 2015.
- [101] S. Shwan, M. Skoglundh, L.F. Lundegaard, R.R. Tiruvalam, T.V. Janssens, A. Carlsson, and P.N. Vennestrøm. Solid-State Ion-Exchange of Copper into Zeolites Facilitated by Ammonia at Low Temperature. *ACS Catal.*, 5:16–19, 2015.
- [102] L.I. Bendavid and E.A. Carter. First-Principles Predictions of the Structure, Stability, and Photocatalytic Potential of Cu<sub>2</sub>O Surfaces. *J. Phys. Chem. B*, 117:15750–15760, 2013.
- [103] C. Paolucci, A. Verma, S. Bates, V. Kispersky, J. Miller, R. Gounder, W. Delgass, F. Ribeiro, and W. Schneider. Isolation of the Copper Redox Steps in the Standard Selective Catalytic Reduction on Cu-SSZ-13. *Angew. Chem. Int. Ed.*, 53:11828–11833, 2014.
- [104] F. Gao, D. Mei, Y. Wang, J. Szanyi, and C.H. Peden. Selective Catalytic Reduction over Cu/SSZ-13: Linking Homo-and Heterogeneous Catalysis. *J. Am. Chem. Soc.*, 139:4935–4942, 2017.
- [105] C. Paolucci, I. Khurana, A.A. Parekh, S. Li, A.J. Shih, H. Li, J.R.D. Iorio, J.D. Albarracin-Caballero, A. Yezerets, J.T. Miller, W.N. Delgass, F.H. Ribeiro, W.F. Schneider, and R. Gounder. Dynamic Multinuclear Sites Formed by Mobilized Copper Ions in NO<sub>x</sub> Selective Catalytic Reduction. *Science*, 357:898–903, 2017.
- [106] P. Vanelderen, J. Vancauwenbergh, B.F. Sels, and R.A. Schoonheydt. Coordination Chemistry and Reactivity of Copper in Zeolites. *A. Coord. Chem. Rev.*, 257:483–494, 2013.
- [107] E.I. Solomon, D.E. Heppner, E.M. Johnston, J.W. Ginsbach, J. Cirera, M. Qayyum, M.T. Kieber-Emmons, C.H. Kjaergaard, R.G. Hadt, and L. Tian. Copper Active Sites in Biology. *Chem. Rev.*, 114:3659–3853, 2014.